

ON THE ABSORPTION AND REDISTRIBUTION OF ENERGY IN IRRADIATED PLANETS

BRAD M. S. HANSEN¹
Draft version June 7, 2018

ABSTRACT

We present a sequence of toy models for irradiated planet atmospheres, in which the effects of geometry and energy redistribution are modelled self-consistently. We use separate but coupled grey atmosphere models to treat the ingoing stellar irradiation and outgoing planetary reradiation. We investigate how observed quantities such as full phase secondary eclipses and orbital phase curves depend on various important parameters, such as the depth at which irradiation is absorbed and the depth at which energy is redistributed. We also compare our results to the more detailed radiative transfer models in the literature, in order to understand how those map onto the toy model parameter space. Such an approach can prove complementary to more detailed calculations, in that they demonstrate, in a simple way, how the solutions change depending on where, and how, energy redistribution occurs. As an example of the value of such models, we demonstrate how energy redistribution and temperature equilibration at moderate optical depths can lead to temperature inversions in the planetary atmosphere, which may be of some relevance to recent observational findings.

Subject headings: line:formation – radiative transfer – atmospheric effects – eclipses – planetary systems

1. INTRODUCTION

The past several years have seen a rapid and exciting increase in the amount of information available concerning the physical properties of extrasolar planets. In particular, the class of short orbital period planets, known informally as ‘Hot Jupiters’, has begun to yield information through a variety of observational channels. The discovery of systems in which the orbital plane is almost edge-on to the line of sight has resulted in the detection of planetary transits (Charbonneau et al. 2000; Henry et al. 2000; Bouchy et al. 2005). Optical and ultraviolet photometry and spectroscopy of such systems can yield information about the absorptive properties of the planet atmosphere (Brown et al. 2001; Charbonneau et al. 2002; Vidal-Madjar et al. 2003; Vidal-Madjar et al. 2004). In addition, the unparalleled capabilities of the Spitzer Space Telescope has allowed the detection of thermal infrared emission (Charbonneau et al. 2005; Deming et al. 2005, Deming et al. 2006; Grillmair et al. 2007; Richardson et al. 2007) during secondary eclipses as well as the measurement of phase curves for non-transiting systems (Harrington et al. 2006).

This flurry of observational activity has spurred a similar level of activity on the theoretical front, with several independent models being used to infer the physical properties of the planets from the observations (Seager & Sasselov 2000; Barman, Hauschildt & Allard 2001; Cho et al. 2003; Menou et al 2003; Sudarsky, Burrows & Hubeny 2003; Burrows, Hubeny & Sudarsky 2005; Dyudina et al. 2005; Cooper & Showman 2005; Seager et al. 2005; Barman, Hauschildt & Allard 2005; Fortney et al. 2005; Fortney 2005; Burrows, Sudarsky & Hubeny 2006; Cooper & Showman 2006; Fortney et al. 2006; Langton & Laughlin 2007). The resulting inferences are not always entirely in agreement. As an example, consider each group’s response to the first detection of secondary eclipses. Burrows et al. (2005) concluded that the redistribution of energy from the substellar to the antistellar face of the planet was weak. On the other hand, Barman, Hauschildt & Allard (2005), as well as Fortney et al. (2005), concluded that the redistribution was strong, while the opinion of Seager et al. (2005) fell somewhere in between. Similarly, predictions for the effects of atmospheric fluid motions on the emergent intensity pattern differ substantially from group to group (Cho et al. 2003; Cooper & Showman 2006; Langton & Laughlin 2007).

This diversity of opinion is hardly surprising, given the complexity of the problem. The study of Hot Jupiter atmospheres requires that we understand the atmospheric chemistry, radiative transfer and hydrodynamics of the planetary atmosphere. These are affected by the thermal structure and evolution of the planet, by the effects of photochemistry induced by ultraviolet light from the star, the possible existence and behaviour of atmospheric condensates, whether they form clouds, and whether (or if) energy is redistributed across the surface of the planet or reradiated in situ. Furthermore, there are a variety of different observational probes, each of which provides information but in ways that differ, sometimes subtly, from other methods. The complexity of the coupled radiative transfer, chemical equilibrium and atmospheric flow models also restrict somewhat the flexibility of the models in providing the true qualitative or geometric information necessary to develop a real understanding of what the observations are telling us.

The overall intent in the pages to follow is pedagogical. Clearly, detailed model atmospheres are necessary to fully interpret the emerging observations. However, simplified models that focus on key physical elements can be useful to try and develop a qualitative understanding of what elements of the model each of the various extant observations is

¹ Department of Physics & Astronomy and Institute of Geophysics & Planetary Physics, University of California Los Angeles, Los Angeles, CA 90095, hansen@astro.ucla.edu

actually probing. To do this, we construct a sequence of analytic and semi-analytic toy models. These models are chosen to be simple enough to be transparent while still capturing the qualitative features of the more detailed models. The hope is that one can use this approach to tailor our interpretations of the more detailed calculations to reach a proper synthesis between theory and the different observations that we have at our disposal. In § 2 we review our simplest model, based on a variation of the grey atmosphere model. In this first case we will assume no redistribution of energy across the face of the planet. In § 3 we then examine how the various available observations relate to the underlying structure of the model. In § 4 we then introduce the physics of energy redistribution into the model and examine how this affects the observations in § 5. Finally, in § 6, we place our models within the context of both observations and more detailed models in the literature, and examine possible implications for future generations of models.

2. MODELS WITHOUT REDISTRIBUTION

To begin, we briefly review the basic steps in calculating the grey atmosphere model. These may be found in almost any textbook on radiative transfer (e.g. Mihalas 1978) but it is worth reviewing them again as we will need to employ some subtle variations in subsequent sections. In doing so we will also derive a simple model which gives an explicit analytic description of the current philosophy in the literature for treating this situation. This will serve as a useful baseline for comparison in later sections.

2.1. The Simplest Model

In the grey approximation, we work with a frequency-integrated version of the radiative transfer equation

$$\mu \frac{\partial I}{\partial \tau} = I - S \quad (1)$$

where I is the specific intensity, and S is the source function. I is a function of optical depth τ and angle cosine (relative to the normal direction) μ . In local thermodynamic equilibrium, where the optical depth is due to absorption rather than scattering, $S = B$, the frequency-integrated Planck function. Integration over angle yields the equation for flux conservation, which is satisfied as long as the conditions for radiative equilibrium are met, i.e. $J = B$. J is the mean intensity, the zeroth moment of I over angle. The first moment of equation (1) yields

$$\frac{\partial K}{\partial \tau} = H \quad (2)$$

where H and K are the first and second moments of I . At this point, we adopt the Eddington approximation, assuming that $J = 3K$. This results in the equation

$$3 \frac{\partial^2 J}{\partial \tau^2} = J - B = 0 \quad (3)$$

which yields a solution for $J(\tau)$, $J = J_0 + J_1 \tau$.

The constant J_1 is determined from equation (2) and the lower boundary condition on the flux $F_{int} = 4H$ entering the atmosphere from below. In the terminology of Mihalas (1978), F is the ‘‘Astrophysical Flux’’ and H is the ‘‘Eddington Flux’’. Since $S = B = J$, one can also determine I from the formal solution to the first order differential equation (1)

$$I(0, \mu) = \int_0^\infty [J_0 + J_1 t] e^{-t/\mu} \frac{dt}{\mu} = J_0 + \frac{3}{4} F_{int} \mu. \quad (4)$$

The final act is to determine the constant J_0 by the calculation of the emergent flux at the surface ($\tau = 0$) from the expression for I and the condition that it must equal F_{int}

$$F_{int} = 2 \int_{-1}^1 \mu I(0, \mu) d\mu = 2 \int_0^1 \mu I(0, \mu) d\mu + 2 \int_{-1}^0 \mu I(0, \mu) d\mu. \quad (5)$$

For most astronomical applications, the second term here is set to zero as it represents the contribution from rays directed inward at the surface, and most stars are not subject to any significant level of irradiation. However, in the case of Hot Jupiters, this particular term is of great importance as it introduces the irradiation from the parent star into the problem. The simple approximation used most often in the literature is uniform irradiation i.e. $I(0, \mu) = I_0$ for $\mu < 0$, although the reality of the situation is that all the incoming rays are coming from a single direction, that of the star. Nevertheless, if we proceed with the uniform irradiation approximation, we can use this to determine J_0 and derive the final solution for the specific intensity

$$I(0, \mu) = \frac{3}{4} F_{int} \left(\mu + \frac{2}{3} \right) + f I_0, \quad (6)$$

where we have included a dilution factor f in the spirit of the more sophisticated modellers. This is how the detailed models attempt to account for the difference between the true situation and the isotropic irradiation assumption. Because of the computation expense involved, these models are still calculated in the one dimensional case, but the

incoming radiation is ‘diluted’ by f in order to approximately mimic the effect of averaging over the true non-uniform irradiation pattern.

An important point to note is that the *net flux* through any given point in the model atmosphere is still only the internally generated F_{int} , since no energy from the irradiation is permanently absorbed by the planet in this baseline model – it is all reradiated. However, the flux the observer sees is the sum total of all flux travelling outwards from the planetary surface, and so includes the contribution of reradiated stellar light. In the case of a secondary eclipse, this is radiated from the surface in the direction of the star. (For this simple model the distinction is moot, but it will become important in subsequent sections).

$$F_{full} = 2 \int_0^1 \mu I(0, \mu) d\mu = F_{int} + f I_0. \quad (7)$$

The traditional assumption found in the literature has been to adopt a value of $f = 1/2$ to represent the case of no energy redistribution over the surface of the planet. In this case the dilution is meant to represent the fact that the incoming flux is absorbed from plane parallel rays spread over over a surface πR_p^2 (where R_p is the planet radius) but is reradiated isotropically from each point on the irradiated hemisphere and so the energy is emitted into a solid angle of 2π . If the energy is redistributed uniformly over the entire planet by fluid motions/winds and only then reradiated, then the angle is 4π and the dilution factor is $f = 1/4$.

2.2. A Better No-Redistribution Model

The previous section gave an explicit example for how irradiated planets are currently treated using a one-dimensional model and a dilution factor. However, we can adapt this formalism easily to treat the geometry of the no-redistribution model properly.

The first improvement to make is to dispense with the assumption of an isotropic irradiation. Consider instead the irradiation is due to a mono-directional beam², so that $I(0, \mu) = I_0 \delta(\theta + \theta_0) \delta(\phi - \phi_0)$ for $\mu < 0$, and θ and ϕ are the poloidal and toroidal co-ordinates for a given point on the planetary surface. Furthermore, we can now choose θ_0 & ϕ_0 so that, for each point on the planet’s substellar hemisphere, the irradiating beam is coming from the direction of the star. To achieve this, we simply note that μ_0 is the angle cosine between the present location and the substellar point. To determine the constant J_0 in this case, we need to match to the outgoing flux $F_{int} + \mu_0 I_0$. With this change, equation (6) is replaced by

$$I(0, \mu_0, \mu) = \frac{3}{4} F_{int} \left(\mu + \frac{2}{3} \right) + \mu_0 I_0 \quad (8)$$

We omit f in this expression because it is no longer needed. This is now a solution that varies across the surface of the irradiated planet, as determined by the local angle of incidence of the irradiation. To obtain the flux we actually observe, we simply integrate over θ and ϕ . Evaluating the integral at full phase (secondary eclipse), we find

$$F_{full} = 2 \int_0^1 \mu_0 I(0, \mu_0, \mu) d\mu_0 = F_{int} + \frac{2}{3} I_0. \quad (9)$$

It is of interest to note that, in order to make equation (7) match this expression, we require $f = \frac{2}{3}$, rather than the value $f = \frac{1}{2}$ that is normally quoted. This is because our new model does not have a uniform distribution of flux over the surface of the planet – rather, it is hotter near the substellar point because that is where the irradiation is the most intense. Thus, the uniform dilution approximation underestimates the secondary eclipse flux.

We can easily confirm global energy conservation in this model. With the monodirectional beam of irradiation, the total flux impinging on the surface of the planet is

$$F_{irr} = 2 \int_0^1 d\mu_0 \left(\int_{-1}^0 \mu I_0 \delta(\mu + \mu_0) d\mu \right) = I_0. \quad (10)$$

Using equation (8) to calculate the total emitted flux returns the same value. In the case of the isotropic irradiation model, the total flux emitted from the planet may be expressed as

$$2 \int_0^1 d\mu_0 \left(2 \int_0^1 \mu I(0, \mu) d\mu \right) = 2F_{int} + 2f I_0 \quad (11)$$

if we use equation (6). The equality of this with F_{irr} is how we arrive at the value $f = 1/2$.

Thus, our very first conclusion, even from a relatively simple model, is that the detailed models in the literature often dilute even their ‘no-redistribution’ models too much. Models for secondary eclipses should not be too democratically averaged over the surface of the planet, but should be weighted in favour of the hotter substellar point. This is in agreement with a similar comparison performed by Barman, Hauschildt & Allard (2005), who compared two

² The readers who are concerned about the use of the Eddington approximation in concert with a monodirectional beam should defer their skepticism until § 2.3. The discussion here is illustrative and this point will be addressed further when we come to the actual model we will use.

dimensional no redistribution models with the same one dimensional models for $f = 1/2$ (their “ α ” is equivalent to our f).

2.3. A Two Opacity Model

We wish to improve our toy model still further, because there is an important piece of physics still missing. The wavelengths of the incoming stellar photons are very different from those of the reradiated photons. This is a consequence of the very different temperatures and hence spectral energy distributions of the star and the planet. The result is that the opacities and hence optical depths can be very different for the energy flow in the optical and infrared wavelength regimes. Thus, we will modify our model such that we treat the absorption of stellar irradiation separately and with a different optical depth than we do the subsequent reradiation.

In order to do this, let us treat the grey version of the radiative transfer equation in a ‘two-stream’ fashion, with two specific intensities, I_1 to describe the optical radiation, and I_2 to describe the infrared radiation. This allows us to treat the two streams with different opacities and emissivities. In this limit, we have two equations of radiative transfer, corresponding to the optical and infra-red respectively.

$$\mu \frac{\partial I_1}{\partial \tau_1} = -I_1 \quad (12)$$

$$\mu \frac{\partial I_2}{\partial \tau_2} = S_2 - I_2 \quad (13)$$

where we have set S_1 , the source function in the optical, to zero, since we assume the planet has negligible emissivity in the optical. Furthermore, the constraint of radiative equilibrium requires that all the energy removed from the beam (in both wavelength regimes) is replaced by the infrared source function S_2 , so that

$$\kappa_1 J_1 + \kappa_2 J_2 = \kappa_2 S_2, \quad (14)$$

where κ_i and J_i are the appropriate opacities and mean intensities³. Thus our radiative equilibrium expression is slightly modified from the usual form,

$$S_2 = J_2 + \frac{\kappa_1}{\kappa_2} J_1 = J_2 + \gamma J_1. \quad (15)$$

Within this approximation, the first moment equations become

$$\frac{\partial H_1}{\partial \tau_1} = -J_1 \quad (16)$$

$$\frac{\partial H_2}{\partial \tau_2} = S_2 - J_2. \quad (17)$$

Using equation (15), and $\tau_1 = \gamma \tau_2$, we can combine these equations into

$$\frac{\partial H_2}{\partial \tau_2} = -\frac{\partial H_1}{\partial \tau_2}. \quad (18)$$

This amounts to the rather obvious statement that all the flux removed from the incoming beam in the optical must emerge in the infrared beam.

The attenuation of the incident beam is described by

$$I(\tau, \mu) = I(0, \mu) e^{\gamma \tau / \mu}, \quad (19)$$

where we have replaced τ_2 with τ , our default optical depth scale henceforth. Recall that $\mu < 0$, since this is an inwardly directed beam. The local flux (travelling inwards) is

$$F = \int_0^{2\pi} \delta(\phi - \phi_0) \int_{-1}^0 \mu I_0 \delta(\mu + \mu_0) e^{\gamma \tau / \mu} d\mu = -\mu_0 I_0 e^{-\gamma \tau / \mu_0}. \quad (20)$$

This is the flux flowing inwards due to the irradiation. We have thus a measure of how much energy is deposited at each depth. We assume the energy is absorbed, thermalised and now reradiated in the infrared. This is done by incorporating equation (20) into equation (18),

$$\frac{\partial H}{\partial \tau} = -\frac{\gamma}{4} I_0 e^{-\gamma \tau / \mu_0}. \quad (21)$$

The gradient in H is negative, because the total energy flux carried outwards by the radiation field is less as one gets deeper into the planet.

³ This approach bears a superficial resemblance to the formalism of Hubeny, Burrows & Sudarsky (2003), in which the two opacities are derived from different frequency averages. However, that study depends critically on the frequency and temperature dependence of the opacity microphysics, as it was focussed on the possibility that multiple solutions might arise for a given physical situation. The multiple solutions derived by Hubeny et al. do not arise in our case, because we assume the opacity ratio γ is a constant.

We once again make the Eddington approximation. This is a poor one for a monodirectional beam, but we note that the approximation is only applied here to the radiation field. Once the energy is thermalised and included in the reradiation energy flow, which is much more isotropically distributed, this is a more reasonable approximation. Thus we obtain the integrable equation

$$\frac{\partial^2 J}{\partial \tau^2} = -\frac{3}{4}\gamma I_0 e^{-\gamma\tau/\mu_0} \quad (22)$$

which can be integrated to yield

$$J = J_0 + J_1\tau - \frac{3}{4}\frac{\mu_0^2 I_0}{\gamma} e^{-\gamma\tau/\mu_0}. \quad (23)$$

The integration constant J_1 is determined, as before, by the internal flux emerging from the planet ($J_1 = \frac{3}{4}F_{int}$). To determine the other constant, we need to ensure the total flux emerging at the top of the atmosphere reflects the appropriate sum of internal and absorbed flux. To that end, we calculate the specific intensity as a function of angle at the surface

$$I(0, \mu_0, \mu) = \int_0^\infty J e^{-t/\mu} \frac{dt}{\mu} = J_0 + \frac{3}{4}F_{int}\mu - \frac{3}{4}\frac{\mu_0^2 I_0}{\gamma(1 + \gamma\mu/\mu_0)}. \quad (24)$$

One may then integrate this over angle to determine the total flux emerging from the surface

$$F = 2 \int_0^1 \mu I(0, \mu) d\mu = J_0 + \frac{1}{2}F_{int} - \frac{3}{2}\frac{\mu_0^3 I_0}{\gamma^2} + \frac{3}{2}\frac{\mu_0^4 I_0}{\gamma^3} \ln\left(1 + \frac{\gamma}{\mu_0}\right). \quad (25)$$

This should match the sum of the internal radiation and flux incident on the top of the atmosphere from the star, $F_{int} + \mu_0 I_0$, so that the final expression for the emergent specific intensity is

$$I(0, \mu_0, \mu) = \frac{3}{4}F_{int} \left(\mu + \frac{2}{3}\right) + \mu_0 I_0 \left[1 - \frac{3}{4}\frac{\mu_0/\gamma}{1 + \gamma\mu/\mu_0} + \frac{3}{2}\left(\frac{\mu_0}{\gamma}\right)^2 - \frac{3}{2}\left(\frac{\mu_0}{\gamma}\right)^3 \ln\left(1 + \frac{\gamma}{\mu_0}\right)\right]. \quad (26)$$

This expression now will allow us to calculate the emergent radiation field in a manner appropriate to any particular observation geometry, given a particular choice of observer orientation and orbital phase. The angle μ_0 measures the angle for each point on the surface relative to the illuminating star, while μ measures the angle relative to the observer. The parameter F_{int} is the internal heat flux emerging from the planet itself, while I_0 encodes the strength of the irradiation. The ratio of I_0 relative to F_{int} will determine whether the observational appearance is dominated by the reradiation of absorbed energy. The one other factor in this equation is γ . This is the ratio of the optical depths for absorbed and reradiated energy. It can be tuned to reflect an optical depth for incoming stellar light that is either more ($\gamma > 1$) or less ($\gamma < 1$) opaque than that for the emerging thermal radiation from the planet. Note that this does not reduce to equation (8) in the case of $\gamma = 1$, because the quantity I now refers only to infra-red light, and so the flux carried in the beam is not constant with depth (as it is in § 2.2).

In the deep absorption limit ($\gamma \rightarrow 0$),

$$I(0, \mu_0, \mu) \rightarrow \frac{3}{4}F_{int} \left(\mu + \frac{2}{3}\right) + \mu_0 I_0 \left[\frac{1}{2} + \frac{3}{4}\mu + \frac{3}{8}\frac{\gamma}{\mu_0} (1 - 2\mu^2)\right] + O(\gamma^2) \quad (27)$$

which can be cast to zeroth order in terms of just an extra contribution to the internal flux, as one would expect

$$I(0, \mu_0, \mu) \rightarrow \frac{3}{4}(F_{int} + \mu_0 I_0) \left(\mu + \frac{2}{3}\right) + \frac{3}{8}\gamma I_0 (1 - 2\mu^2) + O(\gamma^2). \quad (28)$$

In the opposite ($\gamma \rightarrow \infty$) limit (absorption high in the atmosphere), we have

$$I(0, \mu_0, \mu) \rightarrow \frac{3}{4}F_{int} \left(\mu + \frac{2}{3}\right) + \mu_0 I_0 \left[1 + \frac{3}{2}\left(\frac{\mu_0}{\gamma}\right)^2 \left(1 - \frac{1}{2\mu}\right) - \frac{3}{2}\left(\frac{\mu_0}{\gamma}\right)^3 \ln\frac{\gamma}{\mu_0} + O(1/\gamma^3)\right] \quad (29)$$

The last term, despite the logarithmic function of γ , still falls off faster than $1/\gamma^2$, so retaining only the leading term in γ leaves

$$I(0, \mu_0, \mu) \rightarrow \frac{3}{4}F_{int} \left(\mu + \frac{2}{3}\right) + \mu_0 I_0 \left[1 + \frac{3}{2}\left(\frac{\mu_0}{\gamma}\right)^2 \left(1 - \frac{1}{2\mu}\right)\right] + O(\ln \gamma/\gamma^3). \quad (30)$$

So, for high altitude absorption, the zeroth order limit is the simple no-redistribution model of equation 8.⁴

Thus, equation (26) presents us with a simple, yet flexible model that we can use to try and understand how different potential observations probe the properties of Hot Jupiter atmospheres.

⁴ Note that the apparent divergence of the second order term as $\mu \rightarrow 0$ is misleading. One cannot maintain the limit $\gamma \rightarrow \infty$ at the same time as $\mu \rightarrow 0$. One can verify this by taking the appropriate edge-on limit of the full expression, which remains finite.

3. SOME APPLICATIONS

One of the primary goals of this study is to provide a flexible framework in which to understand how the observations probe different elements of the physics. So, let us now consider now how this model is reflected in the various kind of observations that are becoming available.

3.1. Secondary Eclipses

A secondary eclipse occurs when a planet in an edge-on orbit (as measured by the observer) passes behind the star. The size of the flux decrement observed yields the flux emerging from the substellar side of the planet. More specifically, it represents the flux observed at full phase, when $\mu = \mu_0$. Evaluating the emergent flux integral at this phase, we get

$$F_{full} = 2 \int_0^1 \mu_0 I(0, \mu_0, \mu_0) d\mu_0 = F_{int} + \frac{1}{2} I_0 \left[1 + \frac{1}{4\gamma} + \frac{1}{\gamma^2} - \frac{3}{4\gamma(1+\gamma)} + \frac{\gamma}{2} - \gamma^2 - \frac{1}{\gamma^3} \ln(1+\gamma) - \gamma^3 \ln\left(1 + \frac{1}{\gamma}\right) \right]. \quad (31)$$

In principle, comparing the observed F_{full} to model values can tell us whether energy is being redistributed to the antistellar side, because then the observed value would be less than expected from the no-redistribution model. We can express this as an effective value of f by dividing the reradiation term by I_0 , so that

$$f_{eff} = \frac{1}{2} \left[1 + \frac{1}{4\gamma} + \frac{1}{\gamma^2} - \frac{3}{4\gamma(1+\gamma)} + \frac{\gamma}{2} - \gamma^2 - \frac{1}{\gamma^3} \ln(1+\gamma) - \gamma^3 \ln\left(1 + \frac{1}{\gamma}\right) \right]. \quad (32)$$

Despite the algebraic length of the expression, there is actually remarkably little variation as a function of γ . As $\gamma \rightarrow 0$, the limit is

$$f_{eff} \rightarrow \left[\frac{17}{24} + \frac{3}{8}\gamma + O(\gamma^2) \right] \quad (33)$$

while the limit as $\gamma \rightarrow \infty$ is

$$f_{eff} \rightarrow \left[\frac{2}{3} + \frac{3}{5\gamma^2} + O(\ln \gamma / \gamma^3) \right]. \quad (34)$$

Figure 1 shows the function $f_{eff}(\gamma)$. There is only a change of about 6% between high and low values of γ . We may thus conclude that, in case of no energy redistribution, it matters little where in the atmosphere the energy is actually absorbed (at least for secondary eclipse measurements). We find that $f = 2/3$ in the large γ limit, and in the low γ limit, $f = 17/24 = 0.708$. We note that this latter value corresponds to the same full-phase fraction derived by Milne (1926) in his treatment of the ‘reflection effect’ in close binaries. His treatment amounts to a special case ($\gamma = 1$) of the above treatment. The insensitivity of f to γ is encouraging, because it suggests that the comparison of models to secondary eclipse fluxes is robust, in the sense that any flux deficit is likely to indeed be due to the process of redistribution, and not strongly affected by whether the energy is absorbed high in the atmosphere or deep.

3.2. Limb Darkening

Of course, there is much more information potentially available than just the flux at a single orientation. To start, let us consider the planetary limb-darkening law. Neglecting the internal flux term, at full phase we have

$$\frac{I(0, \mu_0, \mu_0)}{I(0, 1, 1)} = \mu_0 \frac{1 - \frac{3}{4} \frac{\mu_0}{\gamma(1+\gamma)} + \frac{3}{2} \left(\frac{\mu_0}{\gamma} \right)^2 - \frac{3}{2} \left(\frac{\mu_0}{\gamma} \right)^3 \ln\left(1 + \frac{\gamma}{\mu_0}\right)}{1 - \frac{3}{4} \frac{1}{\gamma(1+\gamma)} + \frac{3}{2} \frac{1}{\gamma^2} - \frac{3}{2} \frac{1}{\gamma^3} \ln(1+\gamma)} \quad (35)$$

which is shown in Figure 2 for three values of $\gamma = 0.1, 1$ & 10 . Also shown is the normal limb-darkening law for internally generated heat

$$\frac{I(0, \mu_0)}{I(0, 1)} = \frac{3}{5} \left(\mu_0 + \frac{2}{3} \right), \quad (36)$$

and the limb-darkening law derived by Milne (1926) in the two-beam approximation

$$\frac{I(0, \mu_0, \mu_0)}{I(0, 1, 1)} = \left(\frac{1 + 2\mu_0}{3} \right)^2. \quad (37)$$

We see that all the irradiation-driven profiles are much more limb-darkened than the traditional internally generated profile. This is to be expected, since, near the limb, the irradiation is being absorbed at oblique angles and so spread over more area. Absorption high in the atmosphere makes the limb even darker, but the effect is small relative to the dominant effect of the irradiation geometry. The steep dependance on μ_0 is another way to illustrate why the true value of f is $f = 2/3$ rather than $f = 1/2$; the region near the substellar point, which is also the hottest, contributes disproportionately to the reradiated flux observed at full phase.

3.3. Secondary Transit Shapes

During secondary transit, the face of the planet is steadily eclipsed by the star. Thus, the manner in which the total light from the system decreases and increases can, in principle, tell us how light is distributed on the face of the planet. Figure 3 shows the shape of the secondary transit ingress (i.e. the drop in the system flux as the star occults the planet) for three cases. In each case, we assume the occulting body is a sharp, vertical boundary. The solid line indicates a planet with the no-redistribution illumination pattern oriented exactly edge-on. The dotted line is for the same model but now with an inclination of 2 degrees. The dashed line indicates a uniform hemisphere planet oriented exactly edge-on. Each case assumed the planet radius was 0.1 times that of the star and that the orbital semi-major axis is 12 stellar radii. Separating out inclination effects is relatively easy based on the duration of the eclipse, but the measuring differences in illumination pattern by determining the shape of the ingress is going to be quite difficult. The differences are only a few percent at most. This is consistent with other studies concerned with using the shape of secondary transit to infer the presence of non-uniform brightness (Williams et al. 2006; Rauscher et al. 2007a). Greater potential for constraining models is likely to be found in detecting variations in the timing (Williams et al. 2006) or amplitude (Rauscher et al. 2007b) of maximum depth.

Overall then, it appears as though the properties of secondary eclipses are not strongly affected by the value of γ in this model. This is encouraging, since that means we can make robust inferences about the nature of energy redistribution.

3.4. Phase Curves

Another way to probe the asymmetry of the flux distribution emerging from the planet is to measure the phase curve – the variation in the observed brightness of the planet as it orbits the star. For the simplest case, let us consider the phase curve for a planet which has two hemispheres, each of uniform brightness but at different levels. This amounts to a model in the spirit of the default model in § 2.1. Furthermore, let us set the antistellar side to zero brightness, since it is the difference in flux between sub- and antistellar sides that is important.

A location on the surface of the sphere is identified by a unit vector defined in terms of two angles, θ and ϕ ,

$$\hat{\mathbf{n}} = (\cos \phi \sin \theta, \sin \phi \sin \theta, \cos \theta). \quad (38)$$

We consider the direction towards the observer to lie along the x axis, so that the angle cosine between the observer and local normal on the surface of the sphere is then $\mu = \cos \phi \sin \theta$. We also need to specify the direction from which the irradiation comes, using the unit vector

$$\hat{\mathbf{n}}_* = (\cos \lambda \cos i, \sin \lambda, -\cos \lambda \sin i). \quad (39)$$

where the angle λ can circulate in a plane rotated by an angle i about the y-axis. Thus, the angle cosine between this direction and local normal is

$$\mu_0 = \hat{\mathbf{n}} \cdot \hat{\mathbf{n}}_* = \cos \phi \cos \lambda \sin \theta \cos i + \sin \phi \sin \lambda \cos \theta - \cos \theta \cos \lambda \sin i \quad (40)$$

To take account of the phase, we note that we need not account for the true orbital motion, but only the rotation of the irradiation pattern, since the actual orbital displacement is unresolved by any applicable photometric measurement. Thus, our phase curve is described by the circulation of λ . For the edge-on case ($i = 0$) this has an analytic solution for the phase curve

$$F = \int_{-\pi/2}^{\lambda+\pi/2} d\phi \int_0^\pi \sin^2 \theta \cos \phi d\theta \quad (41)$$

for $\lambda < 0$. This applies for brightness of unity for $\mu_0 = \cos(\phi - \lambda) \sin \theta > 0$ and zero otherwise. Evaluation of the integral yields

$$F = \frac{\pi}{2} [1 + \cos \lambda] \quad (42)$$

which also holds for $\lambda > 0$. Figure 4 shows the phase curves for this model and a range of inclinations.

We can repeat the same exercise for the model in § 2.2, except that the surface brightness is no longer uniform, since there is an extra factor of μ_0 in the integrand in equation (41). The solution is then

$$\begin{aligned} F &= \frac{2\pi}{3} \cos \lambda + \frac{2}{3} [\lambda \cos \lambda - \sin \lambda] \quad (\lambda < 0) \\ &= \frac{2\pi}{3} \cos \lambda - \frac{2}{3} [\lambda \cos \lambda - \sin \lambda] \quad (\lambda > 0). \end{aligned} \quad (43)$$

The lower panel of Figure 4 shows the appropriate phase curves. The qualitative difference is that this model has broader troughs and narrower peaks than the uniform hemisphere model. This is a consequence of the concentration of the illumination near the substellar point, so that the phase curve is more sensitive to how this particular region is projected onto the line of sight. Some readers will no doubt note that this is the same as the phase curve for a Lambert sphere (e.g. Russell 1916). Although the Lambert sphere is usually invoked to describe reflected light, the conditions under which it is derived (single, isotropic scattering) amount to the same conditions as applicable to thermal reradiation.

In Figure 5 we show a comparison between these and the phase curves of Barman et al (2005), calculated with a full radiative transfer model for the no-redistribution case. The models show excellent agreement. This suggests that, for reasonable models, the phase curve is determined primarily by the geometry and less by the effects of changing temperature and atmospheric chemistry towards the limb. Indeed, we do not show any phase curves indicating the effect of varying the γ parameter, because the variation is quite small ($\sim 7\%$ change in amplitude between $\gamma = 10^{-2}$ and $\gamma = 100$, with very little change in shape).

3.5. Temperature Profile

We can also calculate the atmospheric temperature structure of these models, using the mean intensity J and the condition of radiative equilibrium, $J = \sigma T^4/\pi$.

$$T = \left(\frac{3}{4}\right)^{1/4} T_{eff} \left[\frac{2}{3} + \tau + \frac{4\mu_0 I_0}{3F_{int}} \left(1 + \frac{3}{2} \left(\frac{\mu_0}{\gamma}\right)^2 - \frac{3}{2} \left(\frac{\mu_0}{\gamma}\right)^3 \ln \left(1 + \frac{\gamma}{\mu_0} \right) - \frac{3}{4} \frac{\mu_0}{\gamma} e^{-\gamma\tau/\mu_0} \right) \right]^{1/4}, \quad (44)$$

where $F_{int} = \sigma T_{eff}^4$. Ideally, we would like to frame this using a quantity more physically useful than I_0 , so we shall define an equivalent temperature by $I_0 = \sigma T_0^4$. Reframing the equation then, we have

$$T^4 = \frac{3}{4} T_{eff}^4 \left[\tau + \frac{2}{3} \right] + \mu_0 T_0^4 \left[1 + \frac{3}{2} \left(\frac{\mu_0}{\gamma}\right)^2 - \frac{3}{2} \left(\frac{\mu_0}{\gamma}\right)^3 \ln \left(1 + \frac{\gamma}{\mu_0} \right) - \frac{3}{4} \frac{\mu_0}{\gamma} e^{-\gamma\tau/\mu_0} \right]. \quad (45)$$

Figure 6 and Figure 7 show the temperature profiles at a range of angles μ_0 , for two cases ($\gamma = 0.1$ and $\gamma = 10$), and assuming $(T_0/T_{eff})^4 = 100$. For the case where energy is absorbed high in the atmosphere the temperature profiles look pretty similar to the unirradiated case, although the asymptotic value of the temperature as $\tau \rightarrow 0$ is higher the closer one gets to the substellar point. In the case where energy is mostly absorbed below the radiative photosphere we find that the temperature profile has two regions where temperature is almost constant – the traditional one at low optical depth but also a second one at $\tau > 1$, where the bulk of the incoming flux is absorbed. This is similar in character to the profiles found in many detailed radiative transfer models (e.g., Seager, Whitney & Sasselov 2000; Barman et al 2005, Burrows, Sudarsky & Hubeny 2006).

The origin of this intermediate plateau is easily understood. The linearity of the equations of radiative transfer and equilibrium means that the above solution corresponds to the superposition of the solutions to two independent problems – the standard solution radiating F_{int} at the boundary with no irradiation plus the solution corresponding to zero net energy transfer with the irradiation boundary condition imposed. As noted by Milne, the temperature profile arising from this latter solution consists of a gentle transition between two asymptotic temperatures (at high and low optical depth). The difference between the two asymptotes is driven by the last term in equation (45), leading to a temperature jump $\Delta T/T_0 = (3\mu_0^2/4\gamma)^{1/4}$, and so is larger for smaller γ . Thus, in Figure 7 we see the behaviour of the zero flux solution at low optical depth and then the transition to the normal thermal profile deeper inside the planet. The same behaviour is found in Figure 6 but the difference between the two asymptotic temperatures is smaller (larger γ) and can barely be discerned in the figure.

3.6. Spectral Lines

The presence or absence of spectral lines in secondary eclipse measurements is a topic of recent excitement (Grillmair et al. 2007; Richardson et al. 2007; Swain et al. 2007). Although our model is founded on the grey atmosphere approximation, we can make simple models of spectral line formation by considering a simple line formation model imposed on the continuum structure represented by our model.

Consider a spectral absorption line resulting from an excess opacity at some specific wavelength. The line opacity at this wavelength is represented by $\tau' = (1 + \alpha)\tau$. We may thus determine the strength of the line using the absorption depth $A = 1 - F_{line}/F_{cont}$, where

$$F_{cont} = 2 \int_0^\infty S(\tau) E_2(\tau) d\tau \quad (46)$$

is the continuum flux, S is the standard source function, and

$$F_{line} = 2 \int_0^\infty S_{line}(\tau') E_2(\tau') d\tau' \quad (47)$$

is the flux at line center. The function $E_2(x) = \int_1^\infty t^{-2} e^{-xt} dt$.

We assume local LTE, so that $S = B = T^4$, and we use the background temperature structure from equation (45). The resulting integration yields the expected $F_{cont} = T_{eff}^4 + \mu_0 T_0^4$. The same calculation to determine F_{line} requires that we replace τ in equation (45) with $\tau'/(1 + \alpha)$ before evaluating the integral. The resulting expression for A , in the limit $T_{eff} \ll T_0$, is

$$A = \frac{3}{2} \left(\frac{\mu_0}{\gamma}\right)^2 \left[\alpha - \frac{\mu_0}{\gamma} \left((1 + \alpha)^2 \ln \left[1 + \frac{\gamma}{\mu_0(1 + \alpha)} \right] - \ln \left[1 + \frac{\gamma}{\mu_0} \right] \right) \right]. \quad (48)$$

In the case of $\gamma \rightarrow 0$ (deep absorption), we find

$$A \rightarrow \frac{1}{2} \frac{\alpha}{1 + \alpha}. \quad (49)$$

In the opposite limit of $\gamma \rightarrow \infty$ (high absorption), we find

$$A \rightarrow \frac{3}{2} \alpha \left(\frac{\mu_0}{\gamma} \right)^2 \rightarrow 0. \quad (50)$$

Thus, we can expect strong absorption lines in the case where the optical opacity is much less than the opacity in the infrared, but weak lines when the optical opacity is large. Similar considerations apply in the case of emission lines ($\alpha < 0$ and $A \rightarrow -A$). Such behaviour is also consistent with the model proposed in Richardson et al. (2007) for example, which invoke TiO or Silicate clouds as sources which can absorb energy at low pressures (high in the atmosphere), in order to explain the lack of observable water absorption.

3.7. Transmission Spectroscopy

Spectral line formation is also relevant to the question of absorption line spectroscopy during primary transit (Charbonneau et al. 2002; Vidal-Madjar et al. 2003, 2004). However, it is somewhat different in detail, since the observation is essentially measuring the attenuation of a parallel beam illuminating and (partially) passing through the limb of the planet. Furthermore, we need to make a further approximation, since the calculation of the transverse optical depth at the limb requires a relation between the physical length scale and the optical depth scale.

We make use of the fact that the absorption occurs high in the atmosphere, where the temperature profile is essentially isothermal. We note, however, that the $\tau \rightarrow 0$ asymptote is still a function of angle from the substellar point. This can be seen from Figure 6 or 7. Assuming that the equation of state is that of an ideal gas, we can approximate the pressure as $P = \rho g H$, where $H(\mu_0)$ is the local scale height. We can then use hydrostatic equilibrium to derive a relation between density and optical depth, so that $\rho = \tau / (\kappa H(\mu_0))$, where τ is still the same local radial optical depth as before. We can then also infer the relationship between optical depth and radial distance r

$$\tau = \tau_0 e^{-r/H(\mu_0)}, \quad (51)$$

where τ_0 is a normalisation constant that can be chosen to fit this approximation (only valid high in the atmosphere) to the true relation. Note that this relationship is a function of angle, so that a surface of constant optical depth is not spherical.

Turning to the optical depth for absorption through the limb, which we denote as τ_ℓ , we have

$$\tau_\ell = 2\gamma \int_0^\infty \kappa \rho dz = 2\gamma \tau_0 \int_R^\infty \frac{e^{-r/H(\mu_0)} r dr}{H(\mu_0) (r^2 - R^2)^{1/2}} \quad (52)$$

where R is the cylindrical radius and so $z^2 + R^2 = r^2$ and $z = \mu_0 r$ (We also include a factor γ to relate this optical absorption to the infrared opacity represented by κ). We can make the evaluation of this integral easier by noting that the scale height is small compared to the radial and cylindrical scales for the atmospheric base. As such, the exponential in the integrand will limit significant contributions to scales such that $r - R \leq H_0$, where $H_0 = H(\mu_0 = 0)$ is the atmospheric scale height at the limb. This comes about because the density drops rapidly as the light path moves away from $\mu_0 = 0$ and results in a negligible contribution to the absorption. With this approximation the integral becomes

$$\tau_\ell = \gamma \tau_0 \left(\frac{2R}{H_0} \right)^{1/2} e^{-R/H_0} \int_0^\infty y^{-1/2} e^{-y} dy = \gamma \tau_0 \left(\frac{2\pi R}{H_0} \right)^{1/2} e^{-R/H_0}. \quad (53)$$

We can see then, that at cylindrical radii R , the optical depth to transmission is $\gamma(2\pi R/H_0)^{1/2}$ larger than the radial optical depth at that location, meaning that the $\tau_\ell = 1$ surface will lie higher in the atmosphere, where $\tau < 1$ (because $R \gg H_0$).

Using equation (53), we can estimate the so-called ‘transit radius effect’ (Baraffe et al. 2003, Burrows et al. 2003), which is the difference between the radius measured by observing a planetary transit, and that calculated in a traditional stellar model (which is usually determined at some fixed radial optical depth τ_f). Setting $\tau_\ell = 1$, to determine R_T , and setting $\tau = \tau_f$ to determine $R_T - \Delta R$, we infer

$$\Delta R = \frac{H_0}{2} \ln \left[\frac{2\pi R_T}{H_0} \gamma \tau_f \right]. \quad (54)$$

Thus, the transit radius increment is proportional to the local scale height at the limb, and only logarithmically dependant on γ or τ_f . Recall that $H_0 \propto T_{eff}/g$, so that there is an inverse relationship with gravity. More surprisingly, there is no direct dependance on the intensity of the illumination, since the asymptotic temperature at the limb ($\mu_0 \rightarrow 0$) does not depend on T_0 . Of course, the irradiation does slow the planet cooling, so that T_{eff} would be higher for the same planet under strong illumination, but this is an indirect effect.

4. ENERGY REDISTRIBUTION

The models in the previous section considered the absorption and re-emission of all radiation locally, i.e. there was no energy transfer between different locations on the planet. However, we have abundant evidence for strong atmospheric flows in our own giant planets and so it is quite possible that winds and atmospheric circulation could redistribute the absorbed energy over a significant fraction of the planet before it is reradiated. This would have a significant influence on the observations, because the no redistribution model leads to large temperature differences between the substellar and antistellar sides of the planet.

4.1. Simplest model

Thus, we turn now to the case of redistribution of energy over the surface of the planet. In this section, we will return to the approximation of § 2.2, wherein we impose the effects of irradiation by use of the outer boundary condition only. We do this in order to isolate the physics of redistribution separately from any considerations about where the energy is actually deposited. In the next section, we will combine our redistribution model with the more detailed γ models outlined in § 2.3. Furthermore, we will assume the redistribution of energy over the surface happens at a single, fixed optical depth τ_w . This introduces a new source/sink term in the radiative transfer equation to reflect the fact that energy may be added or removed from the net flux, depending on location. Equation (3) is thereby replaced by

$$\frac{1}{3} \frac{\partial^2 J}{\partial \tau^2} = -\Lambda \delta(\tau - \tau_w) \quad (55)$$

where Λ is a function (of position on the planet) describing the local energy input/loss due to atmospheric redistribution.

The solution to this equation is of the standard form $J = J_0 + J_1 \tau$ except that now the first derivative experiences a discontinuous jump at $\tau = \tau_w$. Taking into account the internal flux F_{int} we find

$$J = J_0 + \left(\frac{3}{4} F_{int} + 3\Lambda \right) \tau \quad (\tau < \tau_w) \quad (56)$$

$$= J_0 + \frac{3}{4} F_{int} \tau \quad (\tau > \tau_w) \quad (57)$$

As before, we determine the constant J_0 by calculating first $I(0, \mu)$ and using that to calculate the net flux emerging from the surface

$$F = 2 \int_{-1}^1 \mu I(0, \mu) d\mu = 2 \int_0^1 \mu I(0, \mu) d\mu + 2 \int_{-1}^0 \mu I(0, \mu) d\mu \quad (58)$$

$$= -\mu_0 I_0 + 2 \int_0^1 \mu I(0, \mu) d\mu \quad (59)$$

where we have again used as our upper boundary condition for incoming radiation a model in which the incoming radiation is modelled as a beam of intensity I_0 coming from a direction μ_0 . Furthermore, this net flux has to equal the sum of F_{int} and the effect of the Λ term, whether it is positive or negative. Thus, $F = F_{int} + 4\Lambda = F_{int} + \Delta F$. Using this to determine J_0 results in a final answer for the specific intensity of

$$I(0, \mu) = \frac{3}{4} F_{int} \left(\mu + \frac{2}{3} \right) + \mu_0 I_0 + \frac{3}{4} \Delta F \left[\mu(1 - e^{-\tau_w/\mu}) + \frac{2 - 3\tau_w e^{-\tau_w/\mu}}{3} + 2(e^{-\tau_w} - 2E_4(\tau_w)) \right] \quad (60)$$

where $E_n(x) = \int_1^\infty e^{-xt} t^{-n} dt$ is the standard function found in radiative transfer theory and we have made use of the identity $x E_{n-1} = e^{-x} - (n-1)E_n$. In the case of $\Lambda = 0$, this reverts to equation (8).

To model the redistribution, we need to specify the form of the function Λ . We implement redistribution by imposing temperature equilibration on curves imposed by the fluid circulation. Recall that, in LTE, the specific intensity $J = B$, which is the local energy density, so that the redistribution of energy essentially involves equilibration of the mean intensity J around the appropriate curve. In particular, using equation (56), we can calculate J_w , the mean intensity at the optical depth τ_w where redistribution is assumed to occur

$$J_w = \frac{3}{4} F_{int} \left(\tau_w + \frac{2}{3} \right) + \mu_0 I_0 + \frac{3}{4} \Delta F \left[\tau_w + \frac{2}{3} + 2(e^{-\tau_w} - 2E_4(\tau_w)) \right]. \quad (61)$$

To complete the model, we also need to specify the geometry, i.e., along which curve is the temperature equilibrated? There are a variety of models for the fluid circulation on the surfaces of irradiated planets (see § 6.3), and each offers a different possibility. We will base our model on the simulations of Cho et al (2003), who find that the strong winds maintain a banded structure, with a hot equator and cold poles. This is qualitatively similar to the bandedness of Jupiter and other solar system planets, although the bands are fewer and wider because of the different rotational state of the system. Thus, we enforce equilibration of J_w on bands of constant θ_p (the angle measured from the pole of the planet). Recall that the angle cosine μ_0 reflects the angle between the local normal and the direction of the irradiating star. Casting this in terms of angles relative to the pole, yields $\mu_0 = \sin \theta_p \cos \phi_p$. The second term in equation (61) is

linear in μ_0 and so we wish Λ to have a similar dependance in order to cancel out some or all of that angular variation, in the interests of redistribution over ϕ_p for constant θ_p . Thus, we set $\Lambda = \beta_1 + \beta_2 \cos \phi_p$ on the substellar side, and $\Lambda = \beta_1$ on the antistellar side (where we do not need the ϕ_p dependance to cancel out any irradiation term). Energy conservation requires that, if we remove energy at one point on the curve, we must inject it again somewhere else, so that $\int_0^{2\pi} \Lambda d\phi_p = 0$, and so $\pi\beta_1 + \beta_2 = 0$. Furthermore total equilibration requires that all terms in equation (61) that depend on ϕ_p must cancel, yielding an expression for β_1

$$\beta_1 = \frac{I_0 \sin \theta_p}{3\pi \left(\tau_w + \frac{2}{3} + 2e^{-\tau_w} - 4E_4(\tau_w) \right)} \quad (62)$$

and the resulting mean intensity is

$$J_w = \frac{3}{4} F_{int} \left(\tau_w + \frac{2}{3} \right) + \frac{1}{\pi} I_0 \sin \theta_p. \quad (63)$$

The intensity at the surface then follows,

$$I(0, \mu_0, \mu) = \frac{3}{4} F_{int} \left(\mu + \frac{2}{3} \right) + \frac{I_0 \sin \theta_p}{\pi} (1 - \epsilon) + \epsilon I_0 \sin \theta_p \cos \phi_p, \quad (64)$$

where

$$\epsilon = \frac{\tau_w(1 + e^{-\tau_w/\mu}) - \mu(1 - e^{-\tau_w/\mu})}{\tau_w + 2/3 + 2(e^{-\tau_w} - 2E_4(\tau_w))}. \quad (65)$$

This quantity ϵ encapsulates how the surface emission is affected by the depth at which the redistribution occurs. In the limit $\tau_w \rightarrow \infty$, $\epsilon \rightarrow 1$, in which case equation (64) becomes equation (8). This is because, if the redistribution occurs deep in the atmosphere, none of the irradiation actually reaches that depth, and the absorbed energy is reradiated in situ as before. On the other hand, as $\tau_w \rightarrow 0$, $\epsilon \rightarrow \tau_w/2 \rightarrow 0$, and the mean intensity distribution is independent of ϕ_p , although not θ_p , reflecting our approximation that the temperature structure is now banded.

Let us now examine what fraction of the total luminosity is reradiated on the substellar side and the antistellar side. Integrating $F = 2 \int_0^1 \mu I(0, \mu_0, \mu) d\mu$, and then integrating over θ_p and ϕ_p , we calculate

$$L_{sub} = \pi I_0 \left[1 - \frac{2/3 + E_4(\tau_w)}{\tau_w + 2/3 + 2(e^{-\tau_w} - 2E_4(\tau_w))} \right] \quad (66)$$

and

$$L_{anti} = \pi I_0 \left[\frac{2/3 + E_4(\tau_w)}{\tau_w + 2/3 + 2(e^{-\tau_w} - 2E_4(\tau_w))} \right]. \quad (67)$$

We see that $L_{anti} \rightarrow 0$ as $\tau_w \rightarrow \infty$, as expected. As $\tau_w \rightarrow 0$ on the other hand, L_{anti} asymptotes to almost L_{sub} , as expected in the case of complete redistribution. We will postpone calculation of most of the observables until § 5, but we will calculate the expected full-phase flux, as this is the easiest way to estimate whether redistribution is taking place. Recall that to calculate the full-phase flux, we calculate $F_{full} = 2 \int_0^1 \mu_0 I(0, \mu_0, \mu) d\mu_0$, i.e. we impose the condition $\mu = \mu_0$. However, to do this easily, we need to change angular co-ordinate systems. The equilibration was performed on contours that encircle the pole of the planet, but the integration at full-phase is most conveniently performed in angles measured from the substellar point. Thus, let us define the angle ϕ_s as that which circulates about the substellar point, and θ_s the angle relative to that point. As a result, $\sin \theta_p = (1 - \sin^2 \theta_s \sin^2 \phi_s)^{1/2}$. The angle $\mu_0 = \cos \theta_s$ and we can thus perform the integral over θ_s and ϕ_s . Figure 8 shows the resulting flux, expressed in terms of the effective f_{eff} parameter of equation (7). We see that the value tends to the expected no-redistribution value of $2/3$ as $\tau_w \rightarrow \infty$ and comes close to the expected full redistribution value of 0.25 as $\tau_w \rightarrow 0$. The actual asymptotic value is

$$f_0 = \frac{1}{\pi^2} \int_0^{2\pi} d\phi_s \int_0^1 d\mu_0 \mu_0 [1 - (1 - \mu_0^2) \sin^2 \phi_s]^{1/2} = \frac{8}{3\pi^2} = 0.2702. \quad (68)$$

The resulting phase curves are shown in Figure 9. For deep redistribution, the phase curve is very similar to the no redistribution curve, while redistribution at low optical depth suggests almost complete uniformity.

4.2. Redistribution in the γ -model

We now wish to combine the effects of our models in § 2.3 and § 4.1, that is, allow for both a different optical depth in the optical and IR and for redistribution. This will constitute our final model. Thus, equation (3) now has two source/sink terms

$$\frac{\partial^2 J}{\partial \tau^2} = -\frac{3}{4} \gamma I_0 e^{-\gamma \tau / \mu_0} - 3\Lambda \delta(\tau - \tau_w). \quad (69)$$

We follow the same approach as before to derive the mean intensity at τ_w

$$J_w = \frac{3}{4}F_{int} \left(\tau_w + \frac{2}{3} \right) + \frac{3}{4}\Delta F \left(\tau_w + \frac{2}{3} + 2(e^{-\tau_w} - 2E_4(\tau_w)) \right) + \mu_0 I_0 \left[1 - \frac{3}{4} \frac{\mu_0}{\gamma} e^{-\gamma\tau_w/\mu_0} + \frac{3}{2} \left(\frac{\mu_0}{\gamma} \right)^2 - \frac{3}{2} \left(\frac{\mu_0}{\gamma} \right)^3 \ln \left(1 + \frac{\gamma}{\mu_0} \right) \right]. \quad (70)$$

Once again, we wish to equilibrate this quantity on contours of constant θ_p . The functional dependance on ϕ_p is now more complicated than a single cosine, so let us denote the last term as $I_0 \sin \theta_p \Phi(\gamma, \cos \phi_p)$, so that all the variation is contained in the function Φ . Thus, equilibration requires

$$\Delta F = \beta_1 + \beta_2 \Phi \quad (71)$$

to cancel out the variations on the substellar side, while preserving the integral over the contour. Thus

$$\beta_1 = \frac{2}{3\pi} \frac{I_0 \sin \theta_p}{\tau_w + \frac{2}{3} + 2(e^{-\tau_w} - 2E_4(\tau_w))} \left(\frac{1}{\pi} \int_{-\pi/2}^{\pi/2} \Phi d\phi_p \right) \quad (72)$$

$$\beta_2 = -\frac{4}{3\pi} \frac{I_0 \sin \theta_p}{\tau_w + \frac{2}{3} + 2(e^{-\tau_w} - 2E_4(\tau_w))}. \quad (73)$$

We will henceforth denote

$$\langle \Phi \rangle = \left(\frac{1}{\pi} \int_{-\pi/2}^{\pi/2} \Phi d\phi_p \right). \quad (74)$$

The resulting specific intensity at the surface is

$$I(0, \mu_0, \mu) = \frac{3}{4}F_{int} \left(\mu + \frac{2}{3} \right) + \frac{I_0 \sin \theta_p}{\pi} \epsilon \Phi + \frac{I_0 \sin \theta_p}{2\pi} (1 - \epsilon) \langle \Phi \rangle + \frac{3\mu_0 I_0}{4} \left[\frac{\mu_0}{\gamma} e^{-\gamma\tau_w/\mu_0} - \frac{\mu_0/\gamma}{1 + \gamma\mu/\mu_0} \right], \quad (75)$$

where ϵ is defined as in equation (64). This looks much the same as the simpler version, with an extra term on the end that accounts for the fact that the energy is deposited over a range in optical depths, and some may be deposited above τ_w and some below.

We can now calculate how much of the reradiated luminosity is emitted from the substellar side, as a function of γ and τ_w . Figure 10 shows the substellar and antistellar fractions as a function of τ_w for three different cases, $\gamma = 100$, $\gamma = 1$ and $\gamma = 0.01$. At large γ , we see the expected behaviour, where large τ_w implies that very little energy is reradiated on the antistellar side and small τ_w leads to almost complete equilibration. For $\gamma \gg 1$, $\Phi \rightarrow \cos \phi_p$ and the last term in equation (75) is $\sim O(\gamma^{-1})$ even if $\tau_w \rightarrow 0$, so that we recover the same equations as in § 2.1. This tells us that absorption high in the atmosphere can still result in complete equilibration as long as τ_w is relatively small. However, absorption high in the atmosphere results in little equilibration if $\tau_w > 1$.

In the case for $\gamma = 1$ we see qualitatively similar behaviour, except that the solution does not asymptote to complete equality as $\tau_w \rightarrow 0$. The difference is even more extreme for $\gamma \ll 1$. Here we see that there is an intermediate regime ($\tau_w \sim 3$) where almost complete equality is established, but then that solution diverges again as $\tau_w \rightarrow 0$, with fully three quarters of the luminosity emerging on the substellar side. This is because, in the limit $\gamma \rightarrow 0$ (corresponding to deep deposition of energy), the limit of equation (75) is

$$I(0, \mu_0, \mu, \gamma \rightarrow 0, \tau_w \rightarrow 0) = \frac{I_0 \sin \theta_p}{2\pi^2} + \left(\frac{3}{4\pi} I_0 \sin \theta_p \cos \phi_p \right) \mu, \quad (76)$$

in which the second term now behaves like a traditional flux contribution, powered by irradiation energy deposited well below the photosphere. The physical origin of this behaviour is that, in this limit, many photons do not contribute to the temperature at low τ because they are absorbed deep in the atmosphere (because the optical opacity is so low) and then escape from below τ_w (which is small in this limit).

We can summarise the various effects by examining Figure 11, which shows contours indicating the fraction of the total absorbed luminosity that is reradiated on the substellar side. We see that there are two regimes which allow for approximate equality between substellar and antistellar sides. The first is for $\gamma \gg 1$ and $\tau_w \ll 1$. This regime corresponds to the case when both absorption and redistribution both occur high in the atmosphere, as might occur if one has a layer of stratospheric clouds and strong stratospheric winds. The second is the perhaps more traditional case of $\gamma \ll 1$ and $1 < \tau_w < 10$, where energy deposition and energy redistribution occur at moderate (infra-red) optical depths. Note also that the contours tend to change direction near the line $\gamma \sim \tau_w$. Above this line much of the irradiation energy is absorbed in regions of the atmosphere above the redistribution region, while below it the incoming photons penetrate to regions below τ_w before being absorbed.

5. SOME MORE APPLICATIONS

Let us now revisit the various observational probes with our new models and examine how things are changed by the inclusion of redistribution.

5.1. Secondary Eclipses

We can, once again, calculate the full phase flux, as observed during secondary eclipse, using equation (75). Once again, the flux integral is performed with $\mu = \mu_0$. The result is shown in Figure 12, where we have again cast the result in terms of the f_{eff} parameter. We see that, for $\tau_w \gg 1$, we recover the no-redistribution limit for all γ as expected. For a broad range of low and intermediate values of τ_w , the value of f_{eff} varies between 0.4 and 0.5. For low γ , the value of f_{eff} actually has a minimum near $\tau_w \sim 1$. For large γ , the behaviour is more like the simple model, with near complete redistribution at low τ_w , changing monotonically to no redistribution at large τ_w .

The diversity of values obtained demonstrates the complexity of inferring planetary properties from as simple an observation as comparing a flux level at a single phase to the models. We note that the value $f_{eff} = 0.25$ that one expects from the naive full redistribution model is realised only in the $\tau_w \ll 1$, $\gamma \gg 1$ limit and that f_{eff} attains intermediate values ~ 0.4 – 0.6 over most of the parameter space. Thus, while we may be able to demonstrate, using this kind of observation, that a planet possesses some level of redistribution, it will be difficult to determine specific parameters without additional information.

5.2. Phase Curves

This behaviour is also reflected in the diversity of phase curves, shown in Figure 13. The three panels show the phase curves (for edge-on orbits) for three choices of γ . In each panel we show curves for three different τ_w . As expected, large τ_w makes for a strong variation with phase, while low τ_w results in a very flat phase curve. At low γ values, this distinction is blurred somewhat.

Figure 14 summarises this behaviour. We show here the amplitude of the observable phase variation δf , from peak to trough, expressed once again in terms of f_{eff} . We see, not surprisingly, similar behaviour to Figure 12. In the large τ_w limit, we recover $\delta f > 0.6$, essentially no redistribution. On the other hand, amplitudes of $\delta f < 0.1$ are obtainable in the same two regimes as identified above. Once again, intermediate behaviour is recovered over most of the parameter space, with phase variations $\sim 50\%$ of the no-redistribution model expected.

5.3. Limb Darkening

Figure 15 shows the influence of redistribution on the limb-darkening of the planet, when observed at full phase. With the model of redistribution adopted here, the limb is no longer at a constant intensity, but rather shows a variation $\propto \sin \theta_p$. Figure 15 shows contours of the contrast observed at full phase between the intensity at $\theta_p = \pi/2$, $\phi_p = \pi/2$ (the limb at the equator) and the intensity at the center $\theta_p = \pi/2$, $\phi_p = 0$. We see that deep redistribution ($\tau_w \gg 1$) yields low values, indicating strongly darkened limbs, as in the no-redistribution case. We also find dark limbs in the limit $\gamma \ll 1$ and $\tau_w \ll 1$, where the energy is absorbed deep in the star but redistribution occurs high in the atmosphere. However, for $\gamma \gg 1$ (absorption high in the atmosphere), we actually find equality and possibly even limb-brightening. Similar effects have been seen in more detailed models, for instance when the addition of metals results in a large amount of stratospheric absorption (Fortney et al 2006).

5.4. Temperature Profiles

We can also examine the temperature profile. For $\tau < \tau_w$,

$$T^4 = \frac{3}{4} T_{eff}^4 \left(\tau + \frac{2}{3} \right) + T_0^4 \sin \theta_p \left[\left(\left[1 + \frac{\tau - \tau_w}{\tau_w + 2/3 + 2(e^{-\tau_w} - 2E_4(\tau_w))} \right] \frac{\langle \Phi \rangle}{2} + \frac{\tau - \tau_w}{\tau_w + 2/3 + 2(e^{-\tau_w} - 2E_4(\tau_w))} \Phi + \frac{3}{4} \frac{\mu_0 \cos \phi_p}{\gamma} \left[e^{-\gamma \tau_w / \mu_0} - e^{-\gamma \tau / \mu_0} \right] \right) \right]. \quad (77)$$

For $\tau > \tau_w$, the temperature profile still obeys equation (45).

Figure 16 shows temperature profiles for two cases where $\gamma = 100$. In the upper panel, we show the result for shallow redistribution ($\tau_w = 0.1$) and in the lower panel, deep redistribution ($\tau_w = 10$). In each case, the solid curve is the temperature profile at the substellar point ($\theta_p = \pi/2$, $\phi_p = 0$) and the dotted curve is for the limb ($\theta_p = \pi/2$, $\phi_p = \pi/2$). In each case, the ratio $(T_0/T_{eff})^4 = 100$ and the temperature is measured relative to the true internal T_{eff} . In the case of $\tau_w = 10$, the effect of the temperature jumps are largely erased by the time $\tau \rightarrow 0$, presumably because most of the absorbed energy never reaches $\tau = 10$ when $\gamma = 100$. In this case, a temperature inversion is evident, and an important part of the energy balance at moderate τ is thus the transport of energy inwards by thermal radiation from overlying layers heated by the stellar photons. Thus, equilibration at $\tau_w = 0.1$ does a much better job of smoothing out the temperature variations.

In the opposite limit ($\gamma = 0.01$), deep absorption, the temperature profiles are shown in Figure 17. In this case, the opposite behaviour is seen. The deep redistribution case is effective, because most of the irradiation energy is deposited in deeper layers and is included in the thermal balance at $\tau = \tau_w$. In the shallow redistribution case, the temperatures near the substellar point are much hotter at $\tau \sim 1$ and so this case shows a strong asymmetry. There is an interesting center-to-limb temperature inversion at low τ for this case, but it will be difficult to probe with any vertically integrated measures.

5.5. Spectral Lines

We can evaluate the integrals for spectral line formation in a similar fashion as in § 3.6, although the algebra is somewhat more painful this time, and so we will not write the full expression down here. Figure 18 shows the contours of $A = 1 - F_{line}/F_{cont}$ that result from the appropriate integration in the case where $\alpha = 0.3$, for the usual range of γ and τ_w . The calculation is once again at full phase orientation. We see that the strength of the line is relatively weak for $\gamma > 1$ and rather insensitive to τ_w . This is what we expect on the basis of Figure 16, because the temperature profile is close to isothermal. For $\gamma < 1$, the results are more sensitive to τ_w , and can be quite strong in the case where τ_w has a value only slightly larger than unity. This is because the combination of sharp temperature jumps and different opacity scales can lead to large contrasts between line and continuum.

6. DISCUSSION

The overall goal of this exercise is to develop a simple framework within which one can examine the qualitative features of the irradiated atmosphere problem. Clearly, a simple, semi-analytic model such as this cannot replace numerical models that incorporate detailed treatments of radiative transfer, chemical equilibrium (and disequilibrium) and hydrodynamics. However, the complexity of the various physical inputs into these models often results in a situation in which the physical understanding lags behind the calculational output. As a result, simplified models provide a pedagogical framework which can guide the more detailed models. This is likely to be particularly useful as we try to develop physical models for the redistribution of energy within an irradiated planet atmosphere. This is likely to be a difficult and costly enterprise, and the simplified models may help to illuminate the nature of the desired solution and possible pitfalls on the path to their realisation. As a first step, we wish to cast our models in terms of the more detailed models in the literature, in the sense of describing which of our simple models correspond to the more detailed models.

The first attempts to treat the structure of irradiated giant planets (Saumon et al. 1996; Guillot et al. 1996) used essentially grey atmosphere models with a simple asymptotic temperature criterion. The first real attempt to model the radiative transfer under conditions appropriate to Hot Jupiters was by Seager & Sasselov (1998). These models were dust free, and the incoming optical/UV radiation was found to penetrate well below the infra-red photosphere. These models therefore fall into the $\gamma < 1$ category, and establish a theme for most of the subsequent literature. This was followed by Barman, Hauschildt & Allard (2001), who produced two sets of models, “clear”, in which condensates were removed by a rainout process, or “cloudy”, in which the condensates were assumed to form clouds in situ. The cloudy models were found to yield clouds extending from the photosphere upwards to low optical depths, and most likely correspond to the $\gamma > 1$ case. This is supported by the claim that this led to much smoother emergent spectra than in the clear case, as expected for spectral features in the $\gamma \gg 1$ model.

Sudarsky, Burrows & Hubeny (2003) present a variety of models, covering a large range of irradiations. The models they classify as classes IV and V are most appropriate to Hot Jupiters. The majority of their models clearly fall within the $\gamma < 1$ regime. This can best be illustrated by the temperature profiles. Their Figure 12 shows how the temperature profile of a planet changes as it is moved closer to a GOV primary. At distances < 1 AU, the temperature profile develops a plateau at pressures > 1 bar, evolving to a shape very similar to that in Figure 6. For the hottest planets, Iron and Forsterite condensates are possible at high altitude, leading to smaller plateaus, as might be expected for larger γ atmospheres. The clouds in this case are localised, however, and so the analogy with the γ models is not as good as for the Barman et al. (2001) models.

For the purposes of calibration the models of Barman, Hauschildt & Allard (2005) are of particular interest because they calculated a truly two-dimensional model and so produce temperature profiles as a function of angle from the substellar point, rather than just a single ‘representative’ profile. We can thus accurately calibrate the effective γ of their model by making use of the temperature value of the observed plateau in the model. We calibrate T_0 using the known properties of the HD 209458b system, $T_0 = T_{eff}(R_*/a)^{1/2} = 2030$ K. Taking the profile from their Figure 4 for HD 209458b at the substellar point, the high temperature plateau has a value ~ 2500 K. We identify this value with the $\tau \rightarrow \infty$ limit of the irradiation term in equation (45). We use this expression for clarity since the Barman et al. models are for the case of no redistribution, but equation (77) reduces to this in the limit of $\tau_w \rightarrow \infty$. The temperature of this plateau is

$$T^4 = T_0^4 \left[1 + \frac{3}{2} \left(\frac{\mu_0}{\gamma} \right)^2 - \frac{3}{2} \left(\frac{\mu_0}{\gamma} \right)^3 \ln \left(1 + \frac{\gamma}{\mu_0} \right) \right] = 2500^4. \quad (78)$$

We can solve this to infer $\gamma \sim 0.45$ for $\mu_0 = 1$. Figure 19 shows the expression

$$\Upsilon = 1 + \frac{3}{2} \left(\frac{\mu_0}{\gamma} \right)^2 - \frac{3}{2} \left(\frac{\mu_0}{\gamma} \right)^3 \ln \left(1 + \frac{\gamma}{\mu_0} \right) \quad (79)$$

as a function of γ . We see that the inner plateau temperature increases as γ decreases, with the energy getting deposited at greater depth. The lower asymptote for these values of γ and T_0 is derived from $\Upsilon - 3\mu_0/4\gamma$ (shown as the lower curve in Figure 19), and yields a temperature ~ 1800 K. Furthermore, Barman et al. use an internal luminosity effective temperature of $T_{eff} = 230$ K. The resulting temperature profiles are shown in Figure 20. The agreement with Figure 4 of Barman et al is excellent for $\tau > 1$ (corresponding to $P > 10$ mbar). At low optical depths, the temperature drops lower in the detailed models, although it does eventually asymptote to higher temperatures off the edge of the given plot (Barman, private communication). This behaviour presumably reflects the non-monotonic

nature of the real opacity at high altitudes. A general feature of these kinds of model is that (infrared) optical depth unity lies somewhere in the middle of the transition between the two plateau. This can be seen in other models as well, such as from the location of the ‘brightness temperature region’ in Figure 1 of Fortney et al. (2005).

6.1. *Redistribution as dilution*

The detection of secondary eclipses in the HD209458 and TrES-1 systems generated a flurry of theoretical activity. Of particular interest was the question of whether energy was transferred from the day side to the night side. However, all of these models were flux-conserving and so approximate redistribution by diluting the incoming flux by an appropriate factor f . Burrows, Sudarsky & Hubeny (2005) compare their $f = 0.25$ (full redistribution) models to the observed data and find that they are too faint, suggesting that less dilution is best. BSH also express surprise that adding iron or forsterite clouds to their models does not change the predicted fluxes by an appreciable amount. We can understand this by noting that increasing γ at fixed $\tau_w \sim 100$ does not change the predicted f_{eff} , as was noted in § 3.1 and can be seen from Figure 12. Fortney et al. (2005) find that they cannot fit the two IRAC measurements for TrES-1 with a model without redistribution, but are able to almost fit the data with a diluted radiation field appropriate to significant redistribution. The temperature profiles in their Figure 1 suggest again that their model lies in the $\gamma < 1$ regime, with the characteristic two-plateau behaviour very evident. They note that the inclusion of an arbitrary extra continuum opacity in the range 2–6 μm would improve the fit, and which would also move their model to larger γ . Seager et al. (2005) include, as an additional constraint, a limit on the flux variation at wavelengths $\sim 2.2 \mu\text{m}$ (Richardson et al. 2003). This places limits on the depth of observable water bands at near-IR wavelengths. Combining this with the secondary eclipse measurements, they found that the clear ($\gamma < 1$) models were ruled out, but models with thick, absorptive clouds did match the models. In this case clouds composed of Silicates extend from 0.8–5 mbar and Iron condensates from 1.3–10 mbar. From their Figure 4, we can infer directly the approximate γ values appropriate to their models. In the case of the cloud-free models, the optical photosphere lies at greater pressures than the infrared photosphere, and $\gamma \sim 0.1$, while the cloudy model has $\gamma \sim 10$. Similarly Barman et al. (2005) find that their no-redistribution model overpredicts the flux at IRAC wavelengths, so they too infer that some level of energy redistribution must be occurring.

Subsequently, Fortney et al. (2006) have used enhanced metallicity models to predict the structure of the newly discovered hot Jupiter HD149026 b. Their models with 3 times solar metallicity, when calculated in the ‘ 4π ’ (full redistribution) case, have little cloud absorption because the relevant condensation curves lie at pressures of hundreds of bars. In the ‘ 2π ’ (no redistribution) case, the models result in hot stratospheres because the TiO and VO absorption is present at lower pressures for such hot models. The comparison between the resulting temperature profiles can also be understood in the context of our models, since the increase in γ for the no redistribution model leads to a smaller temperature difference between the two plateau, as observed. In this case though, even the hotter model still lies in the $\gamma < 1$ regime.

Burrows, Sudarsky & Hubeny (2006) make a first attempt at predicting phase curves while including a primitive redistribution prescription, in which they remove a fraction P_n of the irradiation energy (i.e. this is still a dilution model) and then incorporate it as an extra internal energy source on the antistellar side. Their temperature profiles again very clearly conform to the $\gamma < 1$ structure we have seen before, consistent with their neglect of clouds. They do, however, discuss one ‘extreme’ model with significant heating of the stratosphere using significant TiO and VO absorption in the upper atmosphere. This may indeed lie with the $\gamma > 1$ regime. Burrows et al present phase curves for a variety of values of P_n and bandpasses, and note that even significant redistribution can still leave some remnant phase variation because of the non-uniform temperature pattern on the substellar side. This has some qualitative resemblance to the kinds of variation seen in Figure 14.

6.2. *Including redistribution in the radiation field directly*

However, all of the previous attempts to model redistribution have relied on some kind of dilution of the original radiation, rather than removal of the energy at the appropriate point in the atmosphere. The models discussed here allow us to examine how the temperature profile changes if we actually include sources and sinks at different points in the atmosphere.

Let us consider the effect of redistribution at different τ_w , using our calibrated version of the Barman et al. (2005) model, shown in Figure 20. Figure 21 shows the effect, on the temperature profile at the substellar point, of moving τ_w to progressively smaller values. Because this is for the substellar point, redistribution removes energy at the specified location, resulting in some pronounced local temperature inversions. In fact, for $\tau_w \sim 10^2$ – 10^4 , there is a pronounced local peak in the temperature, resulting from a competition between the local deposition of irradiation energy and the removal by redistribution. At low enough τ_w , we start to see a significant drop in the stratospheric temperature. The equatorial variation in temperature profile, from center to limb, is shown in Figure 22, for the case $\tau_w = 100$. We see that the effect of redistribution changes from a sink to a source for $\mu_0 < 0.4$, although the general character of a hot substellar point is retained, albeit with reduced amplitude. In the case where $\tau_w = 1$, shown in Figure 23, the temperature at high altitudes is much more uniform.

These effects apply for the case of $\gamma < 1$, which applies to most of the models in the literature. However, there is tentative evidence that some systems may favour the $\gamma > 1$ regime, so let us consider redistribution in this case. First, we show in Figure 24 the effect of changing γ , while keeping all other inputs fixed. The dotted line shows our calibrated model for $\gamma = 0.45$. Lower values of γ result in even higher temperature plateau, as expected, while larger

γ drives the atmosphere closer to an isothermal state. This is precisely why the observed lack of spectral lines favours a high γ model. Figure 25 then shows the effects of different τ_w at the substellar point, but this time for the $\gamma = 10$ model. The temperature jumps are less in this case, but there are still temperature inversions directly above the layer where redistribution occurs. However, the stratospheric temperatures do return to close to their value in the $\tau_w \rightarrow \infty$ case, with large differences only becoming apparent at $\tau_w < 5$. We note, however, that it is precisely this region (large γ , moderate τ_w) that seems to be preferred by the data for HD209458b and HD189733b.

6.3. Hydrodynamic redistribution models

We have thus far discussed the attempts to model energy redistribution in terms of calculations of radiative transfer. A second, and mostly independent, body of work is focussed on the hydrodynamics of irradiated atmospheres and how this might, in turn, influence the redistribution of energy.

The complexity of the physics involved has resulted in somewhat divergent treatments of the phenomenon, each placing emphasis on different aspects of the phenomenon. Showman & Guillot (2002) performed three-dimensional fluid dynamical simulations of the atmosphere, finding the existence of broad east-west jets and strong residual temperature contrasts at the photosphere. Their models also suggested that some fraction of the irradiation energy might get transported deeper into the planet, where it might help to explain the anomalously large radius of HD 209458b. Iro et al. (2005), however, found that very little energy was deposited at pressures > 100 bars. Iro et al. use a coarse version of a one-dimensional radiative transfer model, and include temporally variable forcing to mimic the planetary rotation. However, they do confirm the existence of a strong phase variation within the context of their model, which also fits into the $\gamma < 1$ class of our models. In an updated version of their three-dimensional model, Cooper & Showman (2005) quantify their phase variation, predicting that the equatorial fluid motions should shift the peak of the phase variation $\sim 60^\circ$ downstream, although subsequent revisions of the model quoted in Knutson et al. (2007b) find a smaller phase shift. Similar behaviour is found by Langton & Laughlin (2007). An entirely different approach was taken by Cho et al. (2003; 2008), using a high resolution, two-dimensional model of the fluid equations on a rotating sphere, treated in the shallow water approximation. Cho et al. find generic behaviour in which the principal hydrodynamical feature is a small number of broad equatorial bands, accompanied by coherent polar vortices that rotate about the pole on timescales of several planetary rotation periods. The motion of the temperature field is found to be quite diverse, depending on the strength of the heating and momentum transport in the atmosphere and where the energy is deposited.

Fluid motions are responsible not only for equilibration, but potentially also mixing. Cooper & Showman (2006) showed that hydrodynamic mixing processes can smooth out temperature and compositional differences between different parts of the atmosphere. They predict that this will lead to homogeneous Carbon chemistry, with most of the Carbon residing in CO and very little in CH₄ at low (< 1 bar) pressures. Furthermore, the resulting temperature structure is considerably more isothermal and model spectra show weak features (Fortney et al. 2006), in similar fashion to the observations. It is interesting to consider these latter models in the light of our γ parameter. A uniform vertical redistribution of energy by hydrodynamic mixing can be considered equivalent to uniform absorption throughout the atmosphere, and can lead to a higher effective γ than might be inferred simply from the opacity.

Examination of Fortney et al. (2006) suggests another application of our method. They use a global dynamical simulation of the atmosphere to calculate how the temperature profile varies across the face of the planet and then calculate many one-dimensional radiative transfer models to quantify the likely spectral appearance as determined by the true two-dimensional surface variations. However, they were not able to iterate between the dynamical model and radiative transfer model to achieve a true radiative equilibrium because of the prohibitive computational expense that would entail. A model such as the one described here, suitably parameterised by an effective γ , could be used as an intermediate approximation to enforce a global energetic equilibrium while still retaining the spirit of the radiative transfer model. The resulting temperature distribution could then be used to calculate the detailed appearance.

7. CONCLUSION

In summary, the intent of the models presented here was to understand the qualitative behaviour of radiative transfer in hot Jupiter atmospheres. The simplified nature of the models is dictated by the difficulties of including both full radiative transfer and detailed hydrodynamics, both of which are important parts of a proper understanding of the phenomenon. In particular we have studied how the models change depending on the parameters γ (which reflects the difference in opacity for incoming optical-wavelength radiation and outgoing infrared-wavelength radiation) and τ_w (the depth at which energy is redistributed horizontally across the planets atmosphere).

We have also studied how the various new observational probes of Hot Jupiter atmospheres are influenced by changes in these parameters. We find that models in which redistribution occurs at large infra-red optical depths redistribute little energy to the night side (as expected). Perhaps more surprisingly, we find that significant day/night flux differences can also be found in the case $\tau_w < 1$, as long as $\gamma < 1$ as well. We find that day-side temperature inversions are a generic feature of atmospheres in which the redistribution occurs at moderate ($\tau_w \sim 1-1000$) optical depths. This is of interest because of recent claims that temperature inversions have been found in HD 209458b (Knutson et al. 2007). The initial explanation for such behaviour is high altitude absorption (Burrows et al. 2007; Fortney et al. 2007), although the very low albedo (Rowe et al. 2007) restricts the absorbing species to be a poor reflector. Some level of redistribution is required to explain the HD 209458 b secondary eclipse amplitude and (lack of) phase variations, so that another potential explanation for the temperature inversion may simply be that it is related

to the depth at which the energy is removed from the day-side. Certainly, figures 22 and 23 show that some parts of the planet experience pronounced temperature inversions, even without a significant high altitude absorber. However, it will require detailed radiative transfer models to confirm whether this is a viable model or not.

Our initial exploration has been far from exhaustive. One important advantage of these toy grey atmosphere models is their flexibility, and we have studied how energy redistribution changes the character of the models. This will hopefully provide a guide as to how one might perform similar calculations using the more detailed models, which presently can only consider changes at either the top or bottom of the atmosphere. Furthermore, we have also not exhausted the parameter space of toy models. For instance, one can imagine many other redistribution schemes apart from the one we have implemented here.

This work has been supported in part by NASA ATP contract NNG04GK53G and by funds associated with Spitzer Space Telescope program GO-20101. The author thanks Sara Seager and Travis Barman for helpful comments.

REFERENCES

- Ballester, Sing & Herbert, 2007, *Nature*, 445, 511
 Barman, T. S., Hauschildt, P. H. & Allard, F., 2001, *ApJ*, 556, 885
 Barman, T. S., Hauschildt, P. H. & Allard, F., 2005, *ApJ*, 632, 1132
 Barman, T. S., 2007, *ApJ*, 661, L191
 Baraffe, I., Chabrier, G., Barman, T., Allard, F. & Hauschildt, P., 2003, *A&A*, 402, 701
 Bouchy, F., et al., 2005, *A&A*, 444, L15
 Brown, T. M., Charbonneau, D., Gilliland, R. L., Noyes, R. & Burrows, A., 2001, *ApJ*, 552, 699
 Burrows, A., Sudarsky, D. & Hubbard, W. B., 2003, *ApJ*, 594, 545
 Burrows, A., Hubeny, I. & Sudarsky, D., 2005, *ApJ*, 625, L135
 Burrows, A., Hubeny, I., Budaj, J., Knutson, H. A., & Charbonneau, D., 2007, *ApJ*, 668, L171
 Burrows, A., Sudarsky, D. & Hubeny, I., 2006, *ApJ*, 650, 1140
 Charbonneau, D., Brown, T., Latham, D. & Mayor, M., 2000, *ApJ*, 529, L45
 Charbonneau, D., Brown, T. M., Noyes, R. W. & Gilliland, R., 2002, *ApJ*, 568, 377
 Charbonneau, D., et al., 2005, *ApJ*, 626, 523
 Chauvin, G., Lagrange, A., Dumas, C., Zuckerman, B., Mouillet, D., Song, I., Beuzit, J.-L. & Lowrance, P., 2005, *A&A*, 438, L25
 Cho, J., Menou, K., Hansen, B. & Seager, S., 2003, *ApJ* 587, L117
 Cho, J., Menou, K., Hansen, B. & Seager, S., 2008, *ApJ*, in press; astro-ph/0607338
 Cooper, C. S. & Showman, A. P., 2005, *ApJ*, 629, L45
 Cooper, C. S. & Showman, A. P., 2006, *ApJ*, 649, 1048
 Deming, D., Seager, S., Richardson, L. J. & Harrington, J., 2005, *Nature*, 434, 740
 Deming, D., Harrington, J., Seager, S. & Richardson, L. J., 2006, *ApJ*, 644, 560
 Dyudina, U. A., Sackett, P., Bayliss, D. R., Seager, S., Porco, C. C., Throop, H. B. & Dones, L., 2005, *ApJ*, 618, 973
 Fortney, J. J., Marley, M. S., Lodders, K., Saumon, D. & Freedman, R., 2005, *ApJ*, 627, L69
 Fortney, J. J., 2005, *MNRAS*, 364, 649
 Fortney, J. J., Saumon, D., Marley, M. S., Lodders, K., & Freedman, R. S., 2006, *ApJ*, 642, 495
 Fortney, J. J., Cooper, C. S., Showman, A. P., Marley, M. S. & Freedman, R. S., 2006, *ApJ*, 652, 746
 Fortney, J. J., Lodders, K., Marley, M. S. & Freedman, R. S., 2007, arXiv:0710.2558
 Grillmair, C. J., Charbonneau, D., Burrows, A., Armus, L., Stauffer, J., Meadows, V., Van Cleve, J. & Levine, D., 2007, *ApJ*, 658, L115
 Guillot, T., Burrows, A., Hubbard, W. B., Lunine, J. I. & Saumon, D., 1996, *ApJ*, 459, L35
 Harrington, J., Hansen, B. M., Luszcz, S. H., Seager, S., Deming, D., Menou, K., Cho, J. Y.-K., & Richardson, L. J., 2006, *Science*, 314, 623
 Harrington, J., Luszcz, S., Seager, S., Deming, D. & Richardson, L. J. 2007, *Nature*, 447, 691
 Henry, G. W., Marcy, G. W., Butler, R. P. & Vogt, S. S., 2000, *ApJ*, 529, L41
 Hubeny, I., Burrows, A. & Sudarsky, D., 2003, *ApJ*, 594, 1011
 Iro, N., Bézard, B. & Guillot, T., 2005, *A&A*, 436, 719
 Knutson, H. A., Charbonneau, D., Noyes, R. W., Brown, T. M. & Gilliland, R. L., 2007a, *ApJ*, 655, 564
 Knutson, H. A., et al., 2007b, *Nature*, 447, 183
 Knutson, H. A., Charbonneau, D., Allen, L. E., Burrows, A., & Megeath, T. S., 2007c, arXiv:0709.3984
 Langton, J. & Laughlin, G., 2007, *ApJ*, 657, L113
 Lucas, P. W., & Roche, P. F., 2000, *MNRAS*, 314, 858
 Marley, M. S., Fortney, J., Seager, S. & Barman, T., 2007, *Protostars and Planets V*, B. Reipurth, D. Jewitt, and K. Keil (eds.), University of Arizona Press, Tucson, 951, p733; astro-ph/0602468
 Menou, K., Cho J., Seager S., & Hansen B., 2003, *ApJ*, 587, L113
 Mihalas, D., 1978, 'Stellar Atmospheres', W. H. Freeman & Co.
 Milne, E. A., 1926, *MNRAS*, 87, 43
 Neuhauser, R., Guenther, E. W., Wuchterl, G., Mugrauer, M., Bedalov, A. & Hauschildt, P. H., 2005, *A&A*, 435, L13
 Rauscher, E., Menou, K., Seager, S., Deming, D., Cho, J. & Hansen, B., 2007a, *ApJ*, 664, 1199
 Rauscher, E., Menou, K., Seager, S., Cho, J. & Hansen, B., 2007b, *ApJ*, 662, L115
 Richardson, L. J., Harrington, J., Seager, S., & Deming, D., 2006, *ApJ*, 649, 1043
 Richardson, L. J., Deming, D., Horning, K., Seager, S., & Harrington, J., 2007, *Nature*, 445, 892
 Rowe, J. F., et al., arXiv:0711.4111
 Russell, H. N., 1916, *ApJ*, 43, 173
 Saumon, D., et al., 1996, *ApJ*, 460, 993
 Seager, S., Richardson, L. J., Hansen, B. M. S., Menou, K., Cho, J. & Deming, D., 2005, *ApJ*, 632, 1122
 Seager, S. & Sasselov, D. D., 2000, *ApJ*, 502, L157
 Seager, S., Whitney, B. & Sasselov, D. D., 2000, *ApJ*, 540, 504
 Showman, A. P., & Guillot, T., 2002, *A&A*, 385, 166
 Sudarsky, D., Burrows, A. & Hubeny, I., 2003, *ApJ*, 588, 1121
 Vidal-Madjar, A., Lecavelier des Etangs, A., Désert, J.-M., Ballester, G. E., Ferlet, R., Hébrard, G. & Mayor, M., 2003, *Nature*, 422, 143
 Williams, P., Charbonneau, D., Cooper, C., Showman, A. & Fortney, J., 2006, *ApJ*, 649, 1020

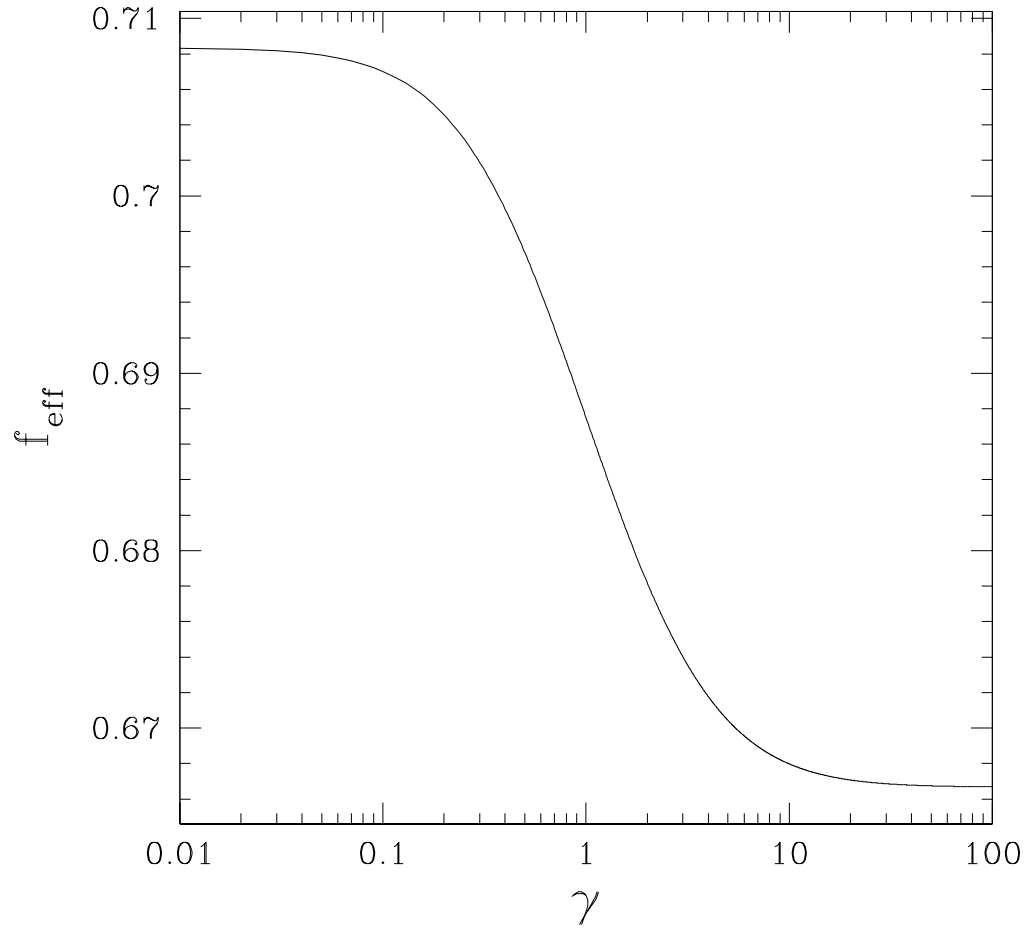


FIG. 1.— The flux observed at superior conjunction, as a function of the energy deposition depth parameter γ , and expressed as an effective value of the parameter f . We see that the value of f_{eff} is rather insensitive to γ .

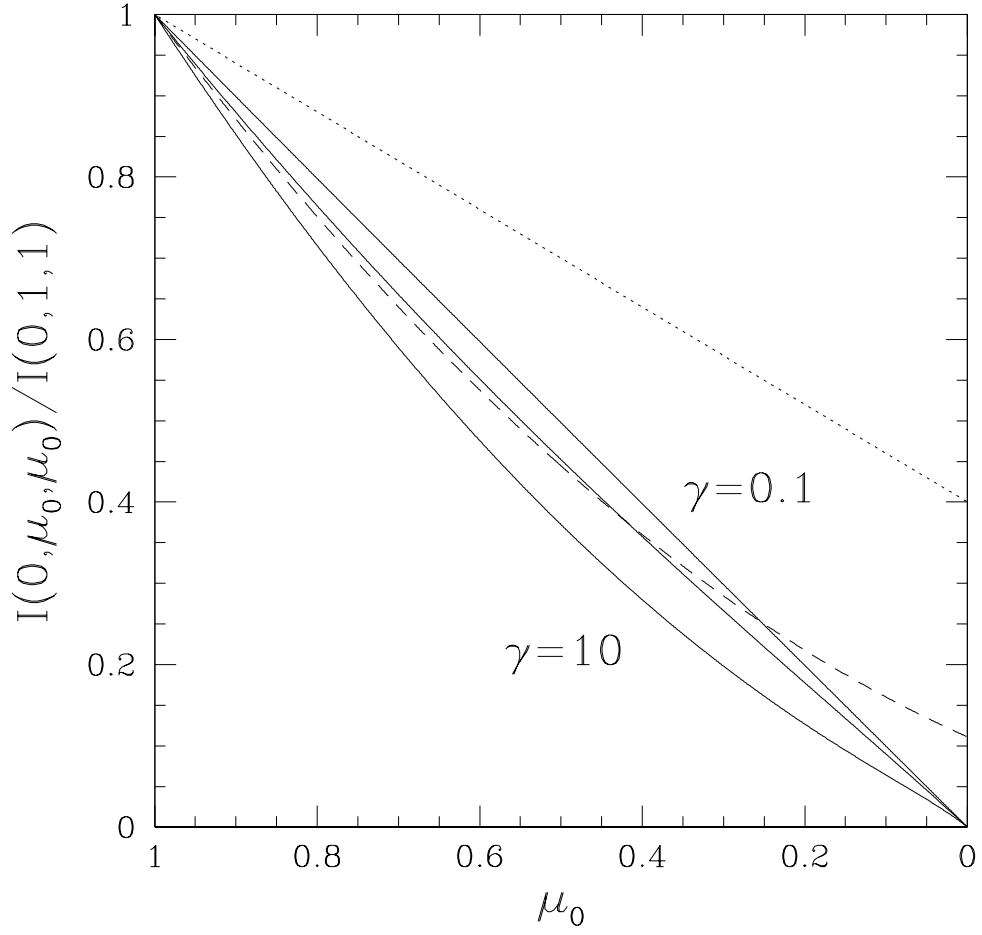


FIG. 2.— The dotted line indicates the normal limb darkening law for an unirradiated grey atmosphere. The three solid lines indicate the same for our irradiated no-redistribution models, for three different values of the deposition depth parameter γ . The values are (from the left) $\gamma = 10$, $\gamma = 1$ and $\gamma = 0.1$. The dashed line represents the expression in Milne (1926), equation 14.

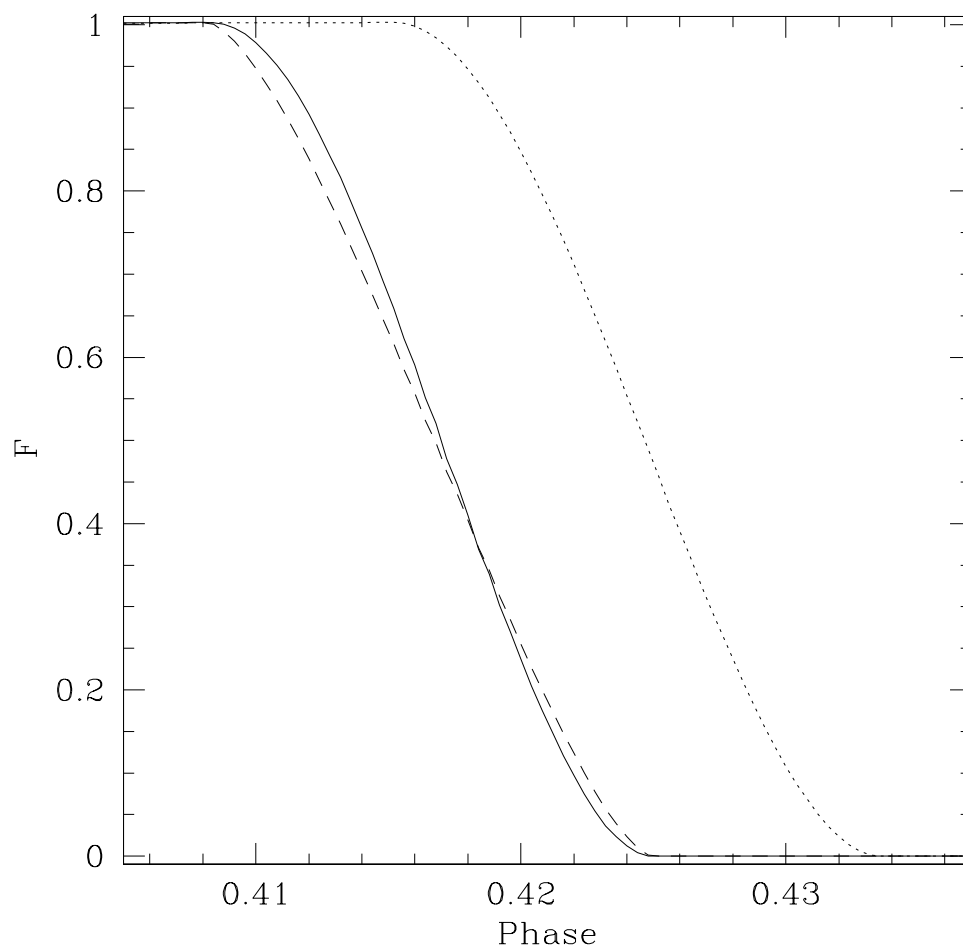


FIG. 3.— The solid and dotted curves represent the secondary eclipse ingress for the no-redistribution model, for zero and 2° inclination respectively. The dashed line is the edge-on ingress for a uniform hemisphere model.

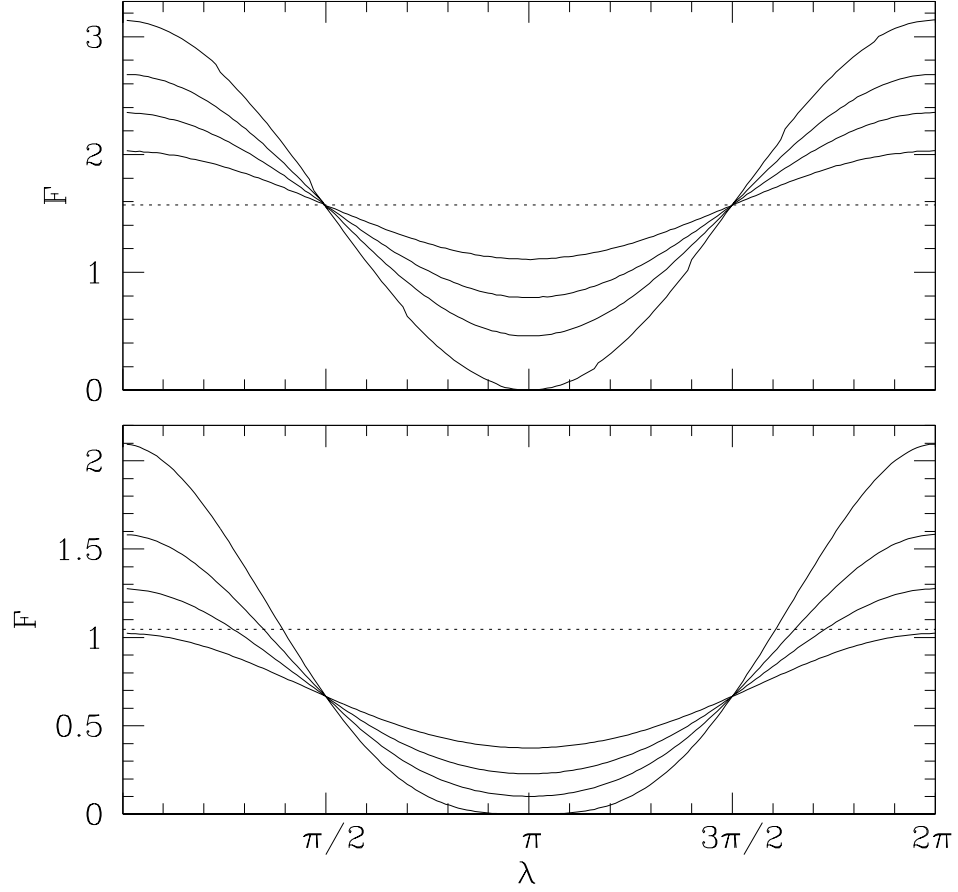


FIG. 4.— The upper panel shows phase curves for the case of the uniformly bright hemisphere model. The lower panel shows phase curves for the case of the no-redistribution model. Curves are shown in each case for inclinations of 0° , 45° , 60° and 75° . The edge-on cases are given by the analytic solutions in equations (42) and (43) respectively.

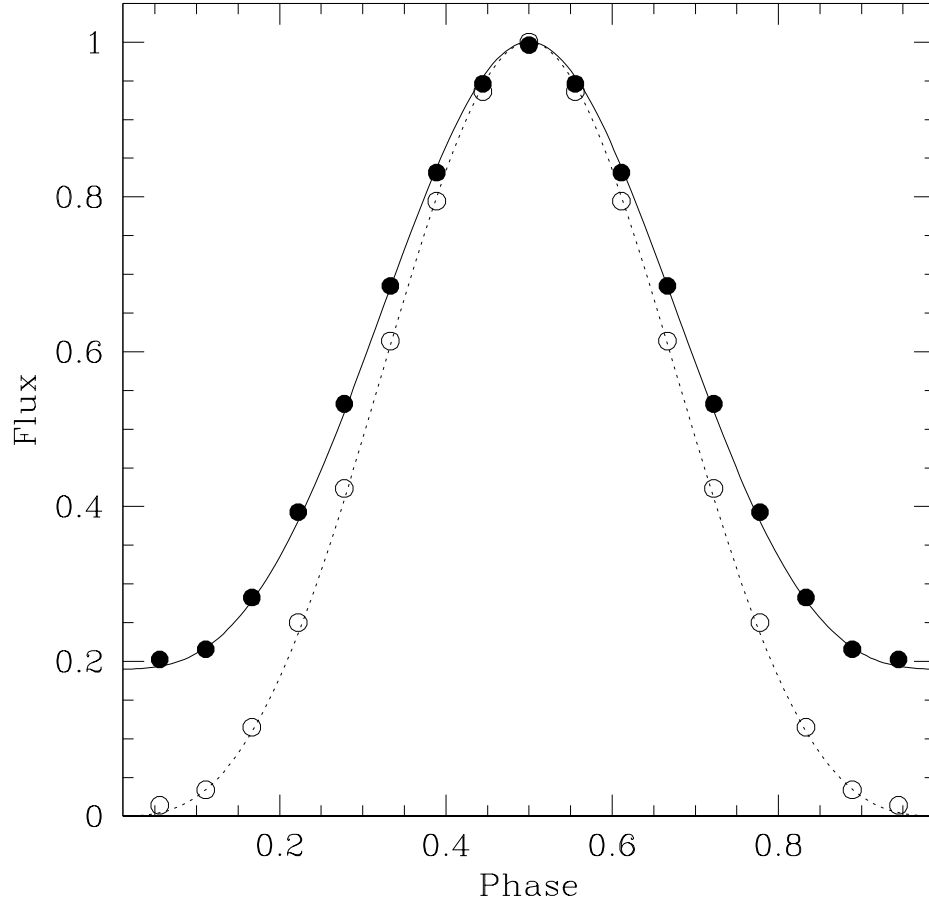


FIG. 5.— The solid and open circles represent phase curves for $24\mu\text{m}$ and $8\mu\text{m}$ respectively, calculated using the models of Barman, Hauschildt & Allard (2005). The dotted line represents the no-redistribution model described in equation (43). The solid line is the same solution, but superimposed on a DC level of 0.19 on this scale, to represent a contribution from internal luminosity. The excellent agreement suggests that the phase curves are determined primarily by geometrical effects.

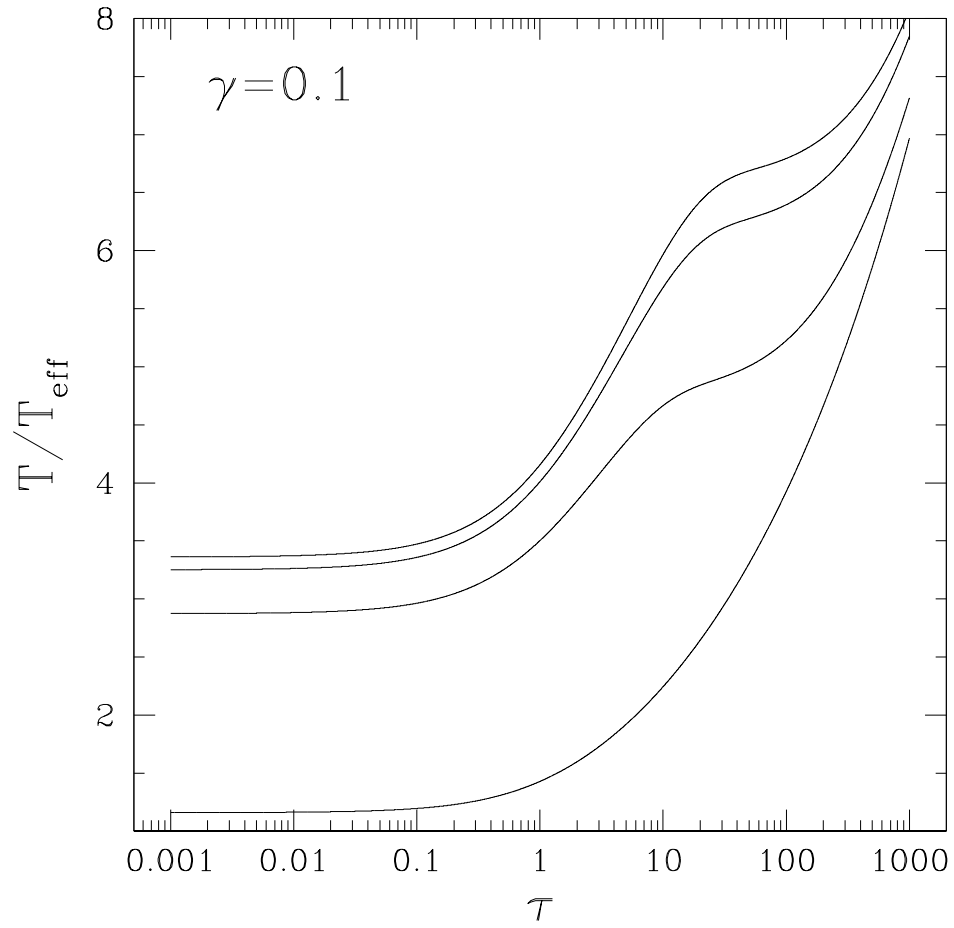


FIG. 6.— The temperature profiles for angles of $0, 30, 60$ and 90° to the line of sight, for the case $\gamma = 0.1$, i.e. where the irradiation penetrates to below the reradiation photosphere. We have also used $(T_0/T_{\text{eff}})^4 = 100$.

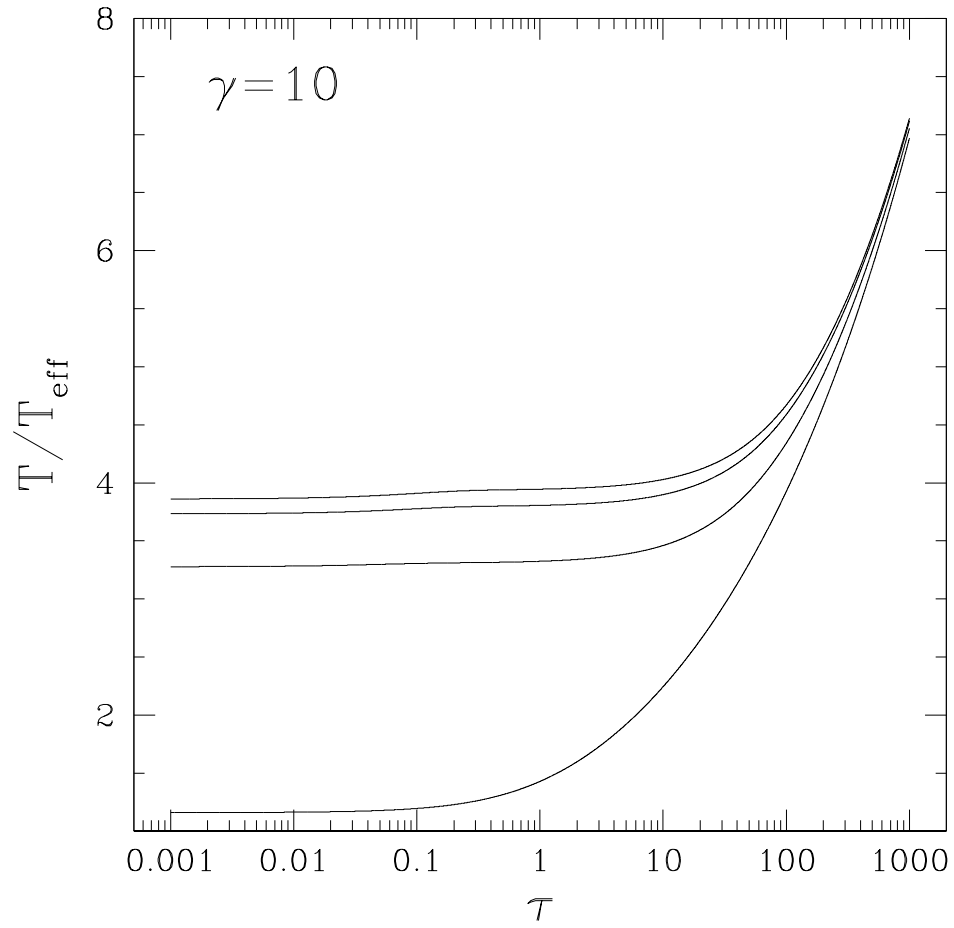


FIG. 7.— The temperature profiles for angles of $0, 30, 60$ and 90° to the line of sight, for the case $\gamma = 10$, i.e. where the irradiation is absorbed high in the atmosphere. We have also used $(T_0/T_{\text{eff}})^4 = 100$.

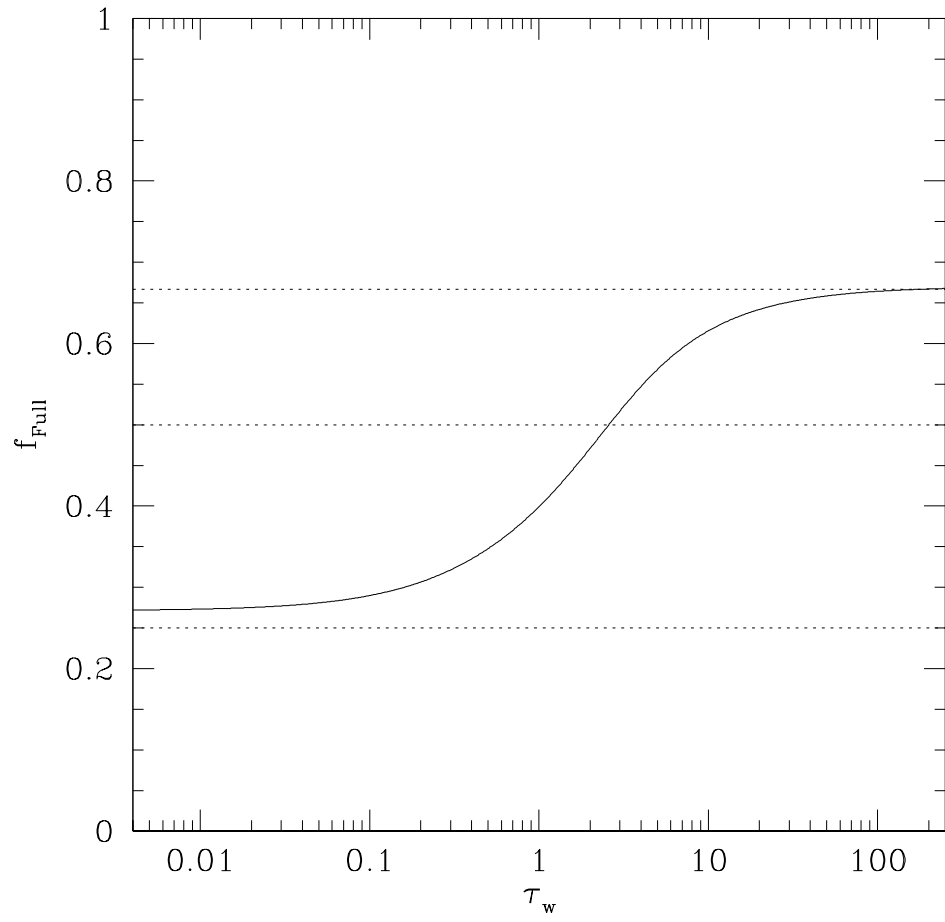


FIG. 8.— The solid curve shows the effective f value for the full phase flux in our complete redistribution model, as a function of the redistribution depth τ_w . The dotted lines indicate the canonical values of 0.25, 0.5 and 2/3 discussed in the text.

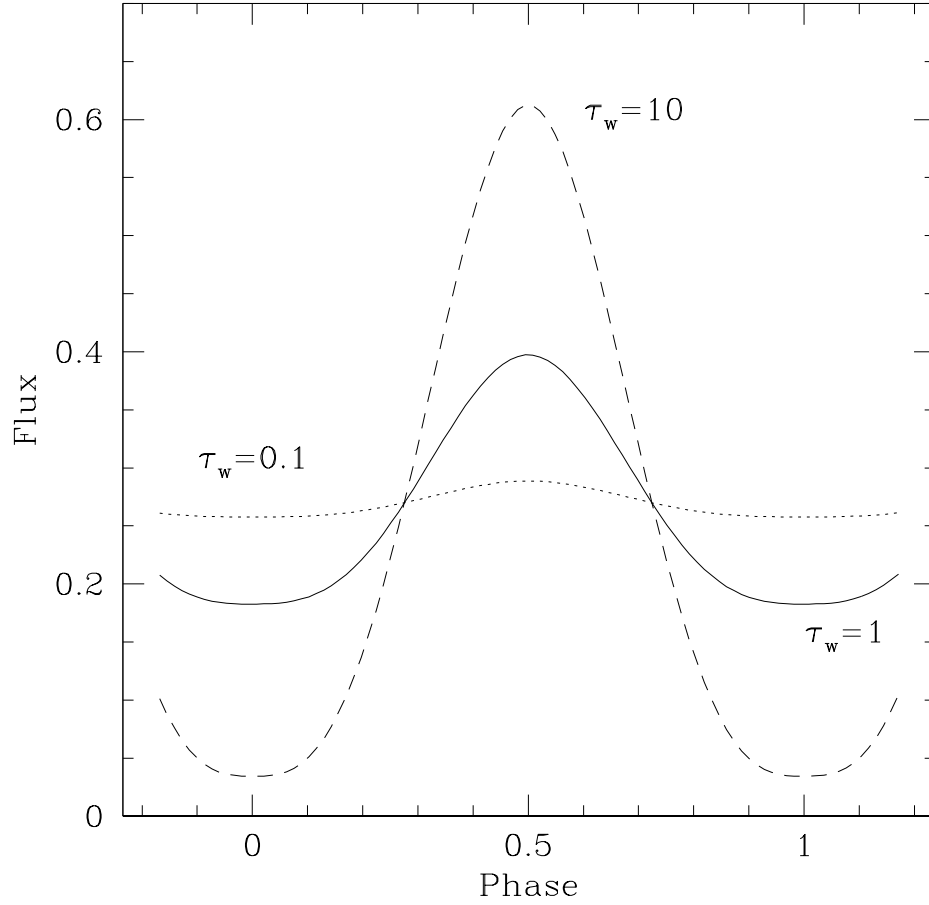


FIG. 9.— The solid line represents the phase curve for a planet in an edge-on orbit in which the redistribution occurs at $\tau_w = 1$. The dotted and dashed lines indicate the same, but for $\tau_w = 0.1$ and $\tau_w = 10$. One can observe the transition from almost no redistribution to almost complete uniformity as τ_w decreases. The flux level is parameterised in terms of effective f .

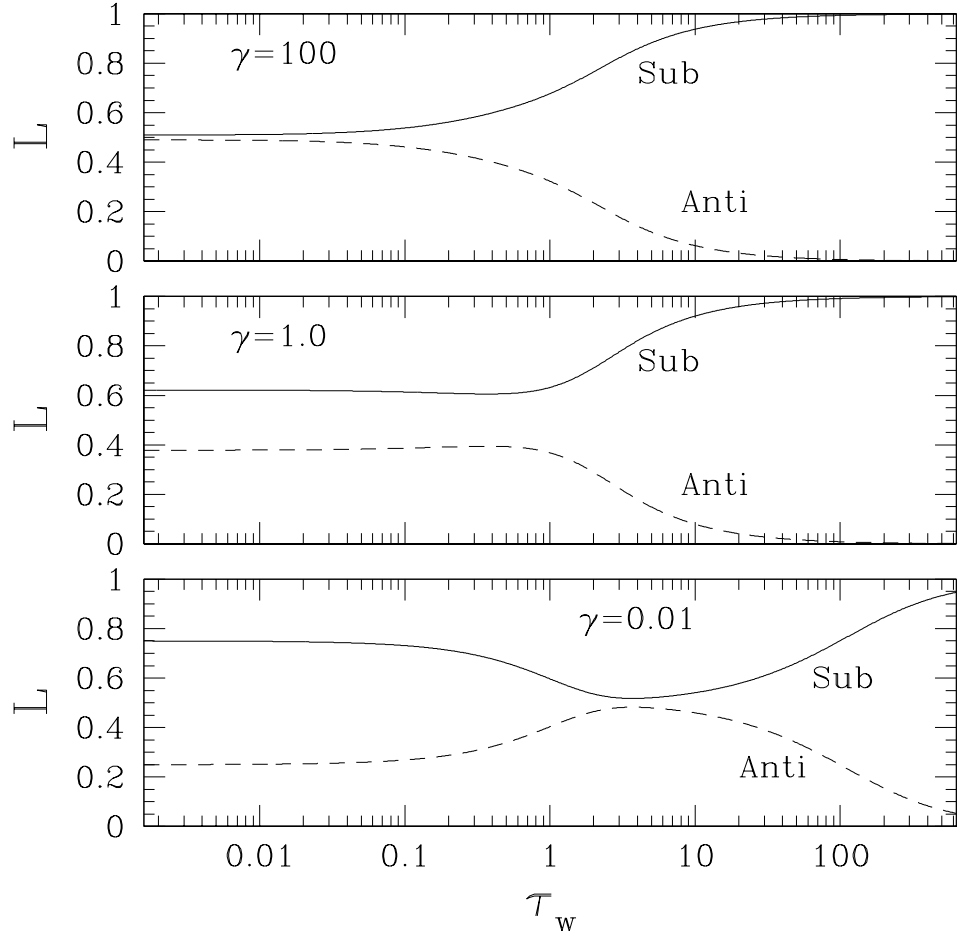


FIG. 10.— The three panels show how the relative luminosity of the substellar and antistellar sides vary with τ_w , for three different values of γ . For large γ (upper panel), we see a smooth transition from complete redistribution at low τ_w to essentially no redistribution at large τ_w . For lower values of γ however, the dependence is more complicated.

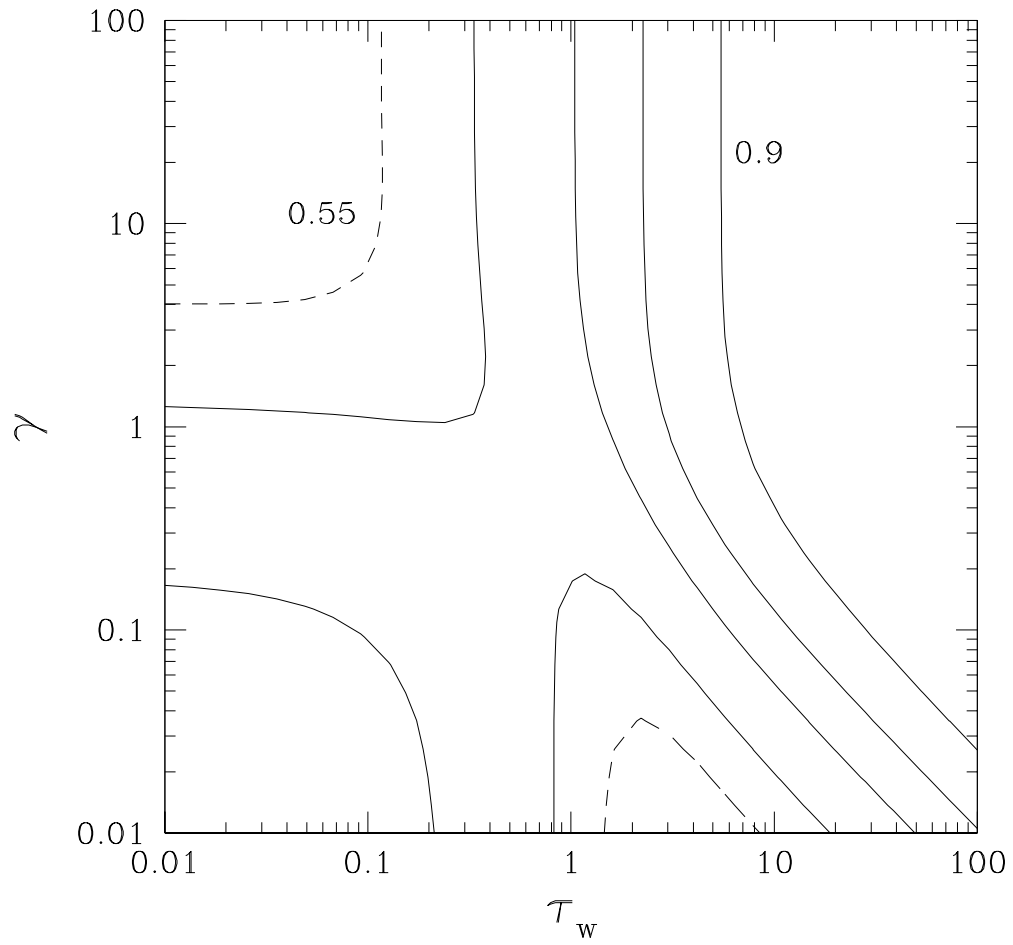


FIG. 11.— The solid lines are contours of L_{sub}/L_{total} , ranging from 0.6 to 0.9. The dashed contour is a value of 0.55. These latter contours enclose that region of the phase space where the energy is approximately evenly redistributed.

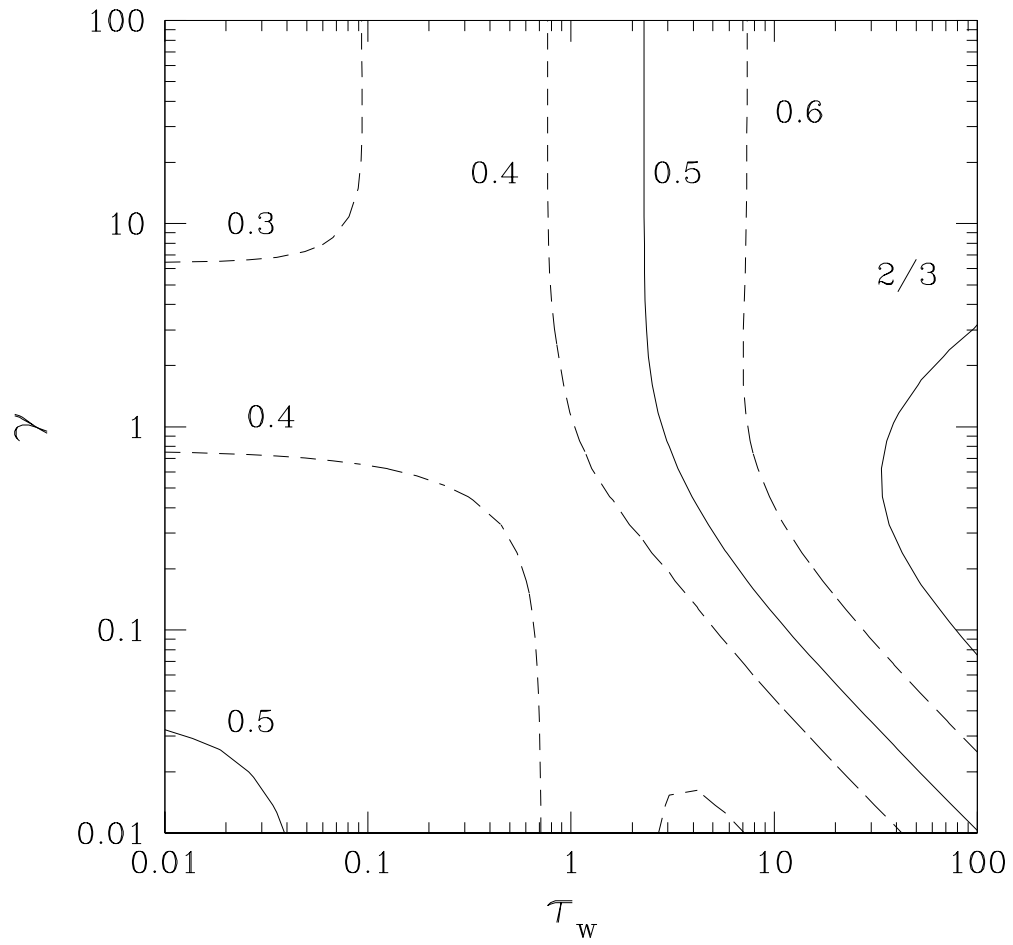


FIG. 12.— The solid contours indicate values of the full-phase scaling parameter f that correspond to canonical values $1/2$ and $2/3$. Dashed curves indicate other values as labelled.

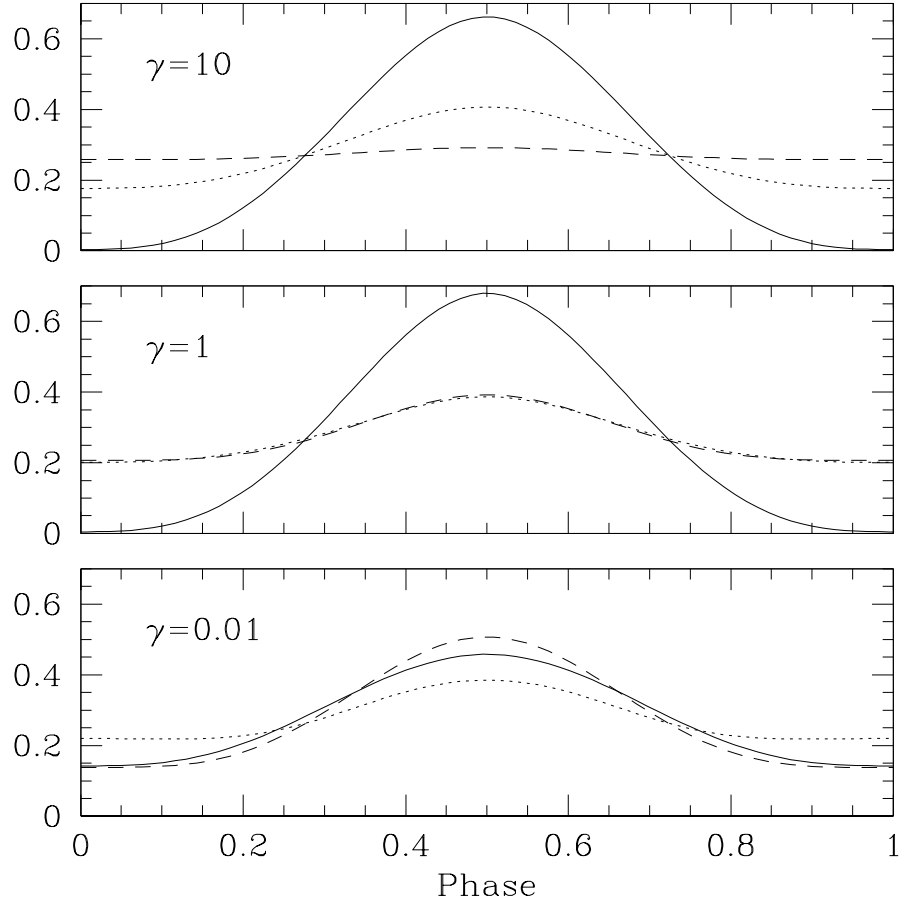


FIG. 13.— In each panel, corresponding to a different value of γ as labelled, the solid curve indicates $\tau_w = 100$, the dotted curve $\tau_w = 1$ and the dashed curve $\tau_w = 0.01$. In the middle panel, the dotted and dashed curves lie very close to one another. The nature of the phase curve can be seen to depend clearly on both γ and τ_w .

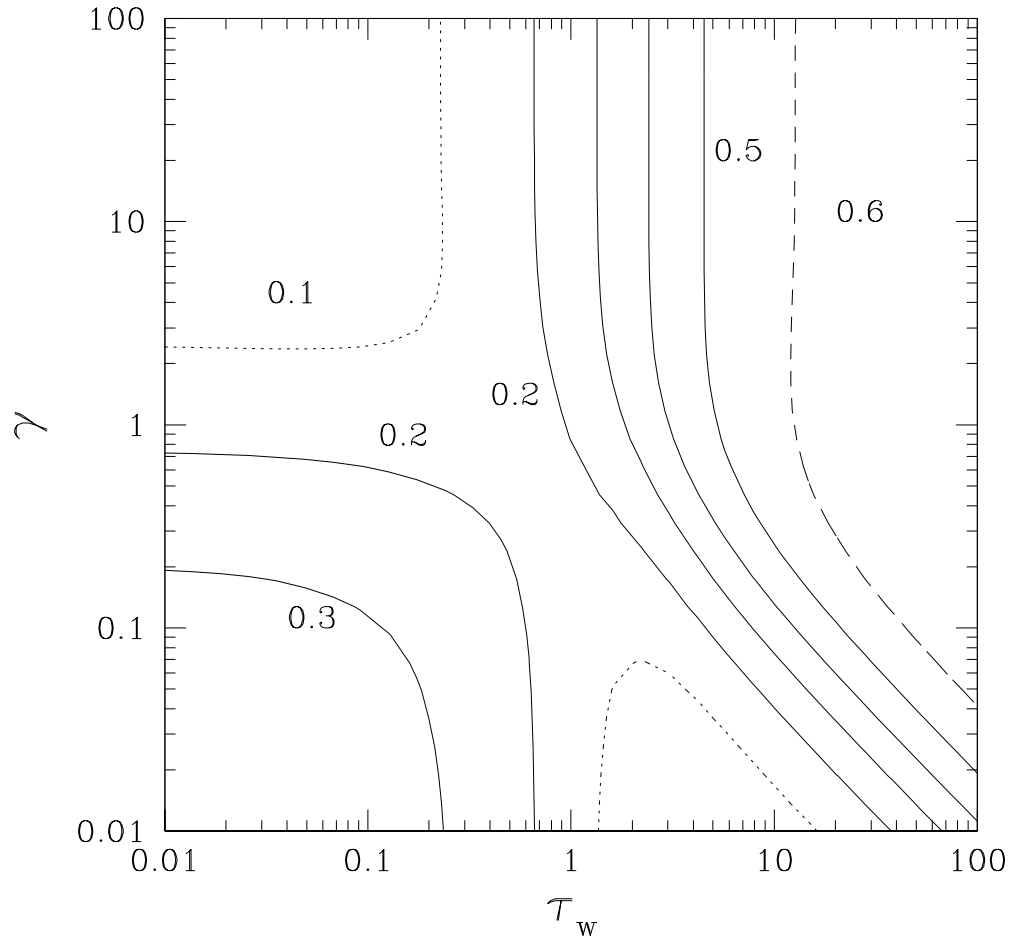


FIG. 14.— The contours plotted here are for the quantity δf , which is the difference in f_{eff} when observed at full phase and zero phase. We have assumed an edge-on orbit here. The dotted and dashed curves represent $\delta f = 0.6$ and $\delta f = 0.1$ respectively. The solid contours lie between these two values, in increments of 0.1. We see that phase variations of moderate amplitude are expected over a wide range of parameters.

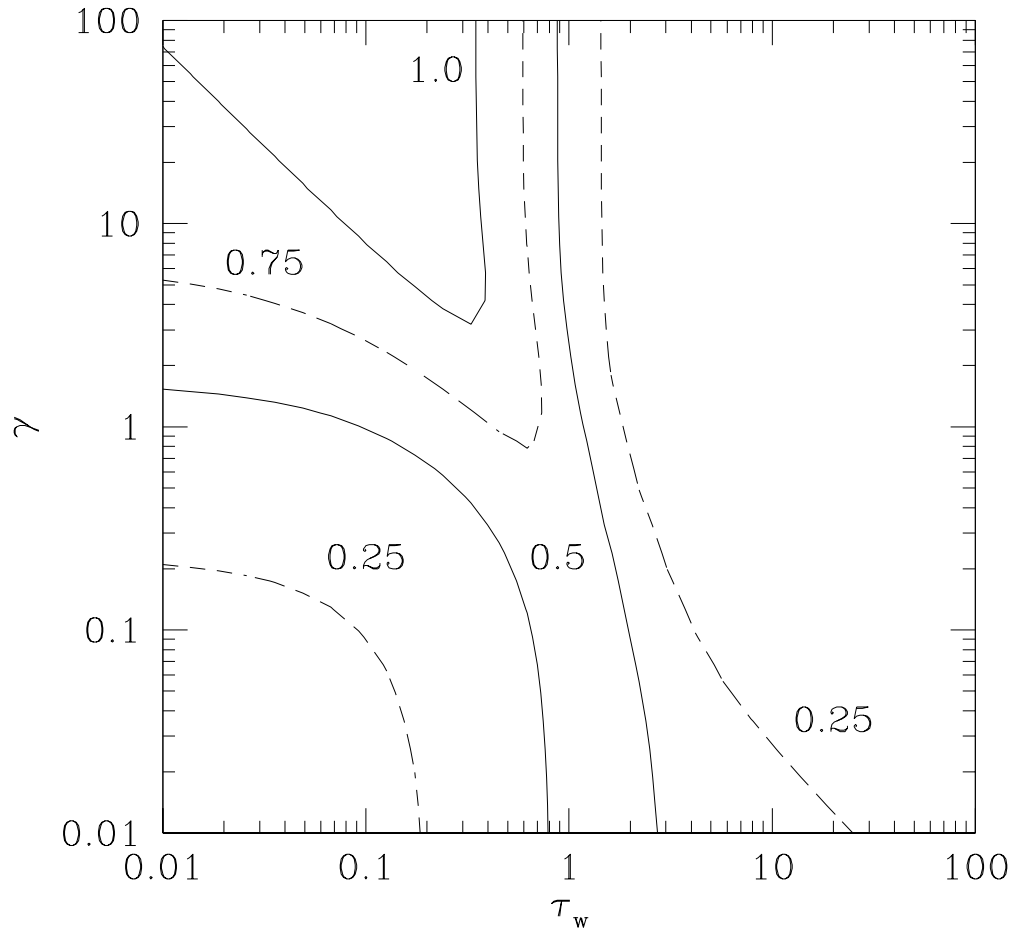


FIG. 15.— The contours indicate ratios of the intensity at the equator limb to the intensity at the substellar point, when the planet is observed at full phase. The solid contours indicate values of 0.5 and 1.0, while the dashed contours are 0.25 and 0.75. We see that deep redistribution indicates strong limb darkening, while high altitude absorption with moderately shallow redistribution can actually lead to limb brightening.

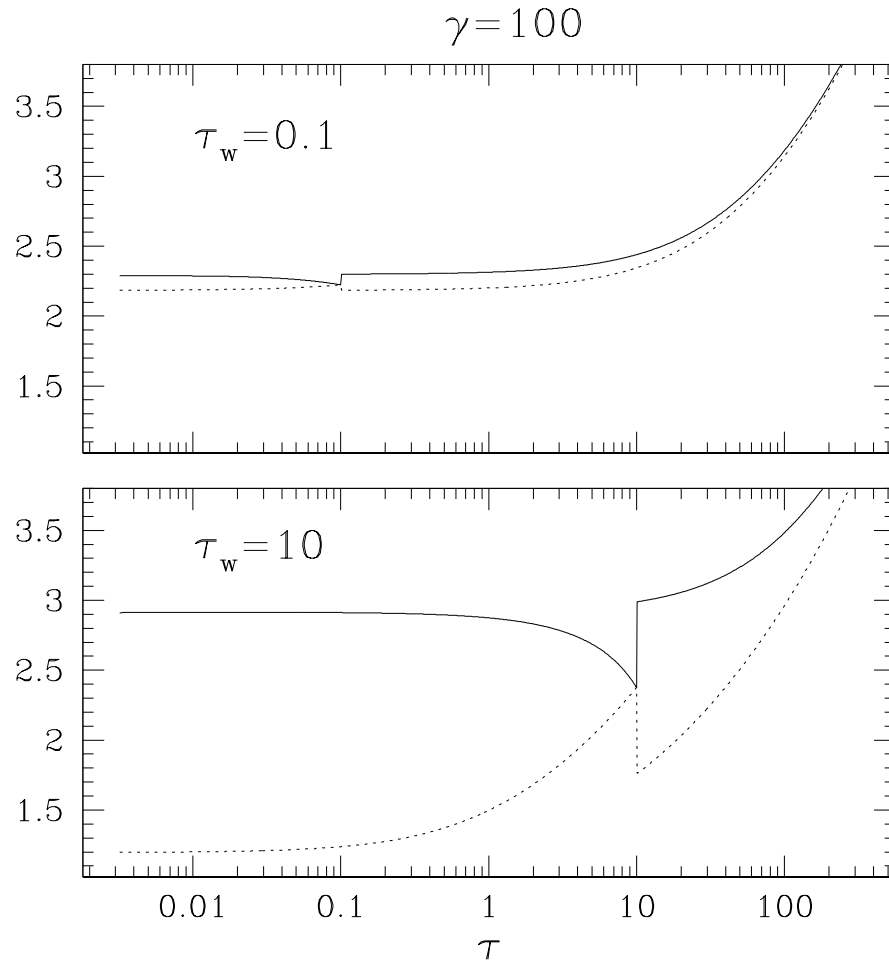


FIG. 16.— The solid lines show the temperature profile for the substellar point in each case. The dotted lines indicate the temperature profile at the limb (for $\theta_p = \pi/2$). The upper panel indicates redistribution is efficient in the case for low τ and large γ but inefficient for large τ and large γ .

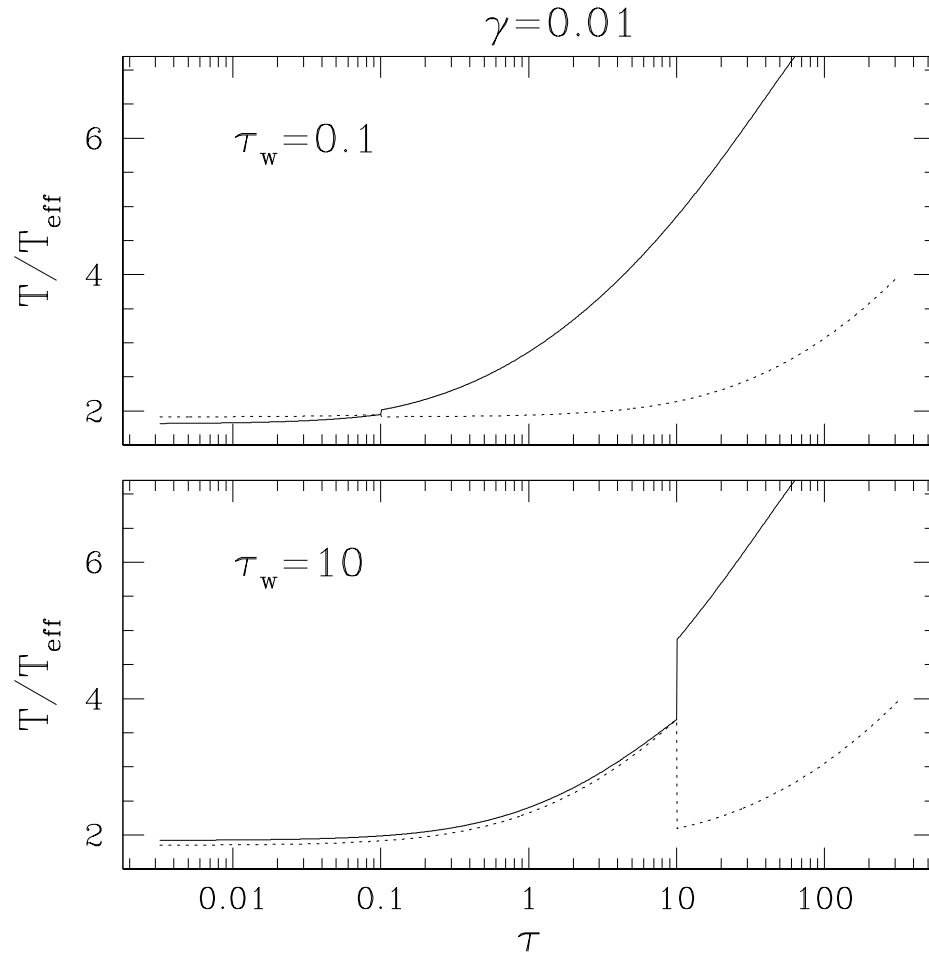


FIG. 17.— The solid lines show the temperature profile for the substellar point in each case. The dotted lines indicate the temperature profile at the limb (for $\theta_p = \pi/2$). The upper panel indicates redistribution is inefficient in the case for low τ and low γ but efficient for large τ and small γ .

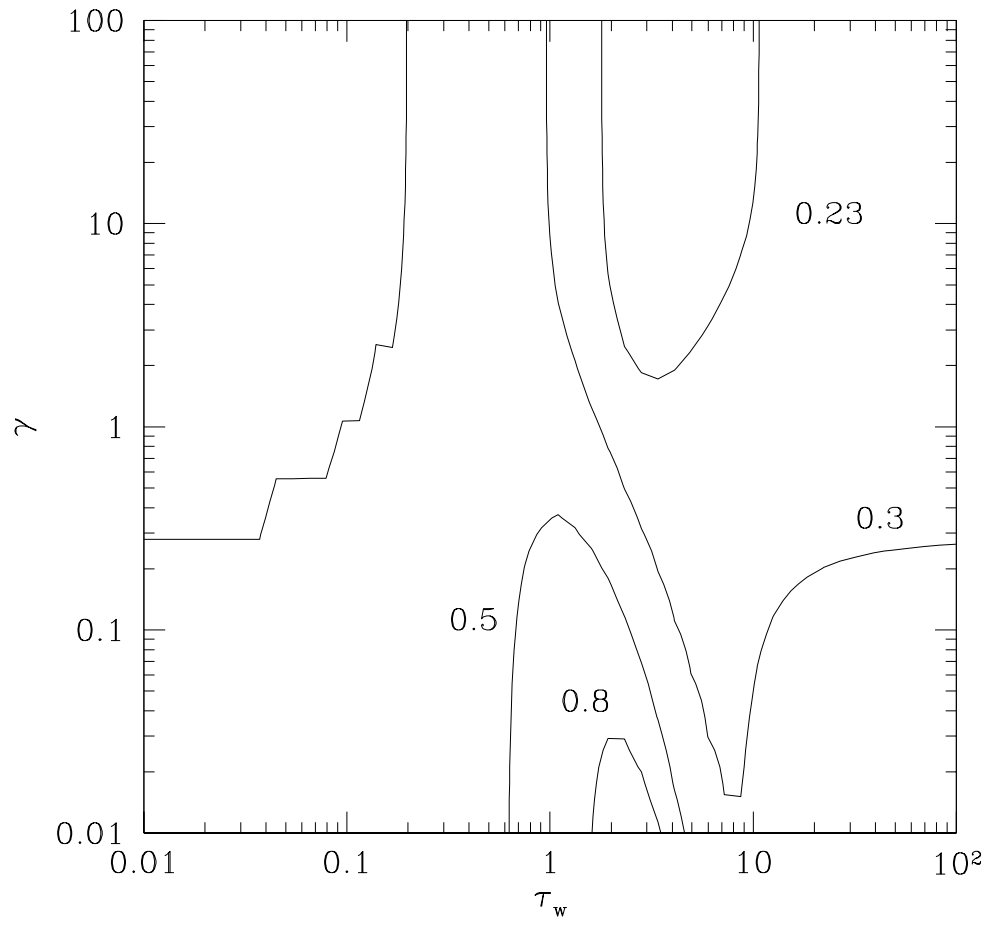


FIG. 18.— The solid contours indicate values of spectral line strength A . We see that the strongest lines occur for $\gamma \ll 1$ and $\tau_w \sim 2$. For $\gamma > 1$, the lines are relatively weak and show little dependence on τ_w .

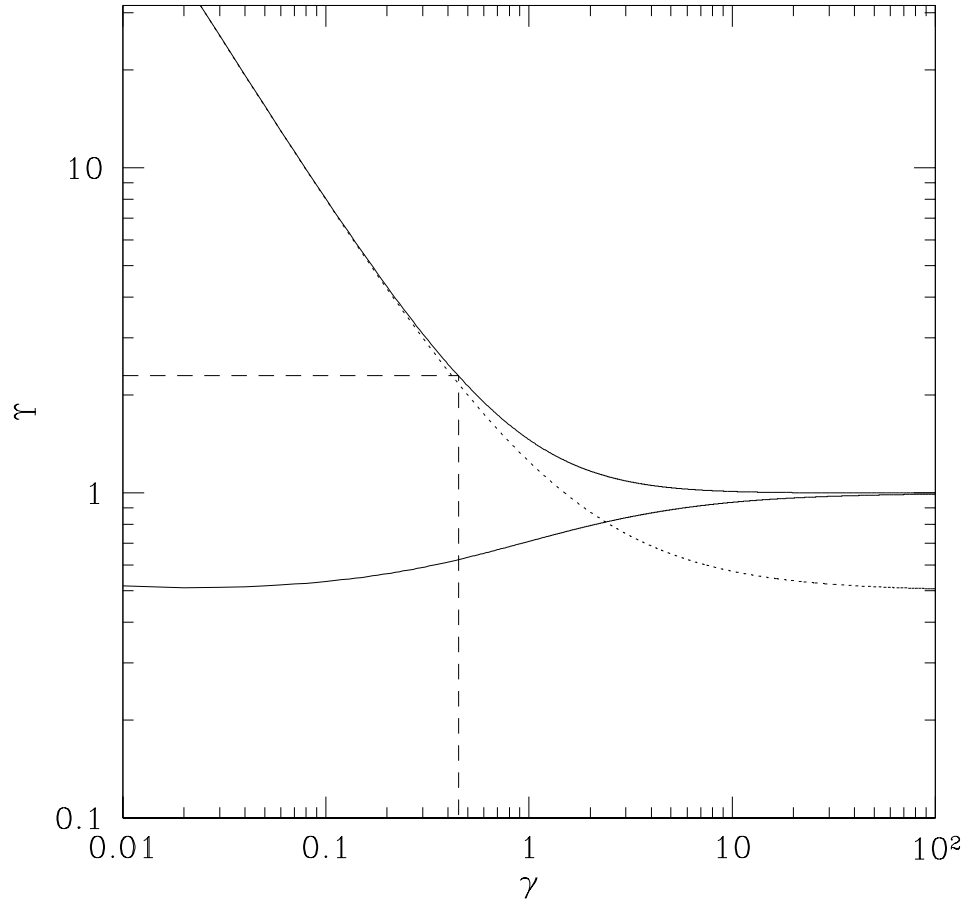


FIG. 19.— The upper solid line is the function $\Upsilon(\gamma)$. For $\gamma \ll 1$, the function asymptotes to $\rightarrow 1 + 3/2\gamma$, indicated by the dotted line. The dashed line corresponds to the solution for the Barman et al. (2005) case. The lower solid line is the corresponding function for the lower temperature plateau in our simple model.

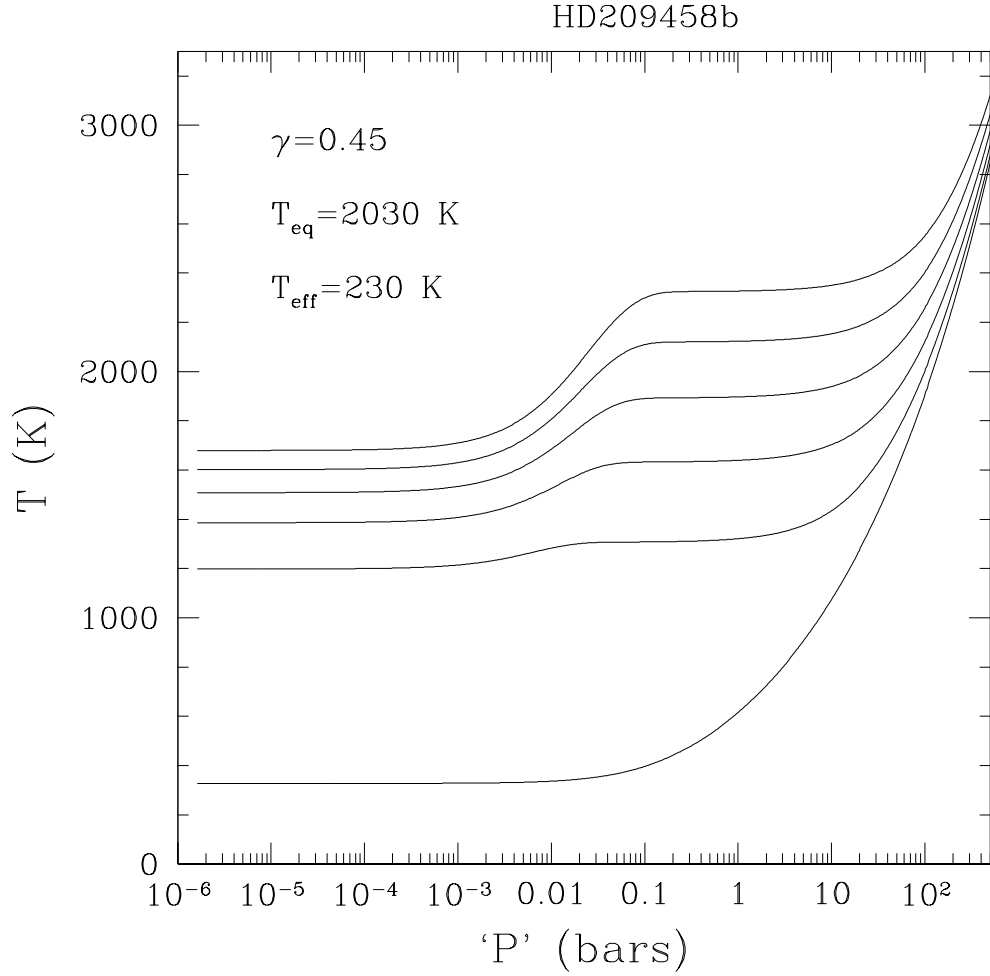


FIG. 20.— The solid curves show the temperature profiles for $\mu_0 = 1.0, 0.8, 0.6, 0.4, 0.2$ and 0 (from top to bottom). The value of $\gamma = 0.45$ was chosen to match the normalisation of the models of Barman et al. (2005). The other parameters T_0 and T_{eff} were chosen based on the values used by Barman et al. The horizontal axis is really τ , but we have scaled this down by a factor 63 to mimic pressure in bars. (We expect the scaling to be linear for a plane parallel atmosphere with constant opacity. In fact, using the known gravity of HD 209458b, we can even derive the effective mean IR opacity $\sim 0.07 \text{ cm}^2 \text{ g}^{-1}$).

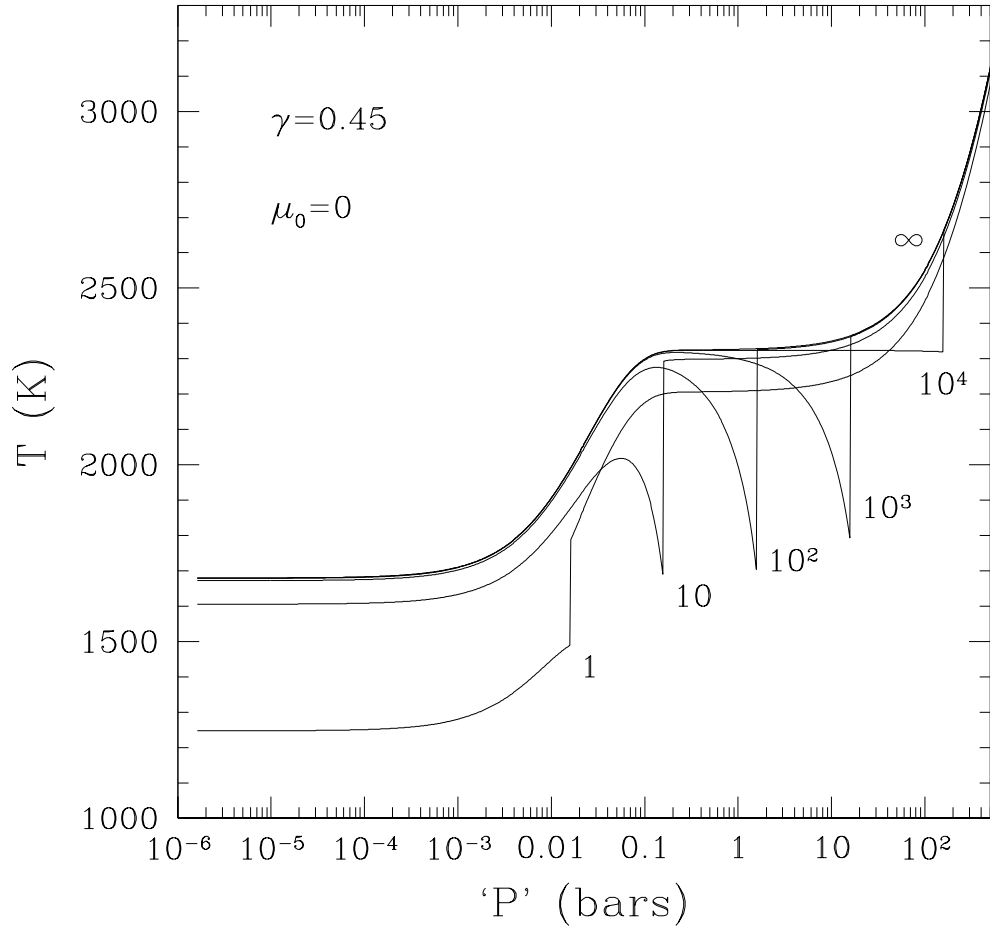


FIG. 21.— The curves show how the temperature profile of the $\gamma = 0.45$ model at the substellar point changes as we decrease τ_w , the optical depth of the redistribution layer. Each curve is labelled with the appropriate value of τ_w . The effect of redistribution at the hottest point on the star is clearly to remove energy and transport it to cooler parts of the star. Thus, we see depressions in the temperature profile near τ_w . However, for values of $\tau_w \sim 10^2$ – 10^4 , we see that this region lies in the middle of the temperature plateau where much of the energy is being absorbed. The combination of these two effects leads to conspicuous temperature bumps.

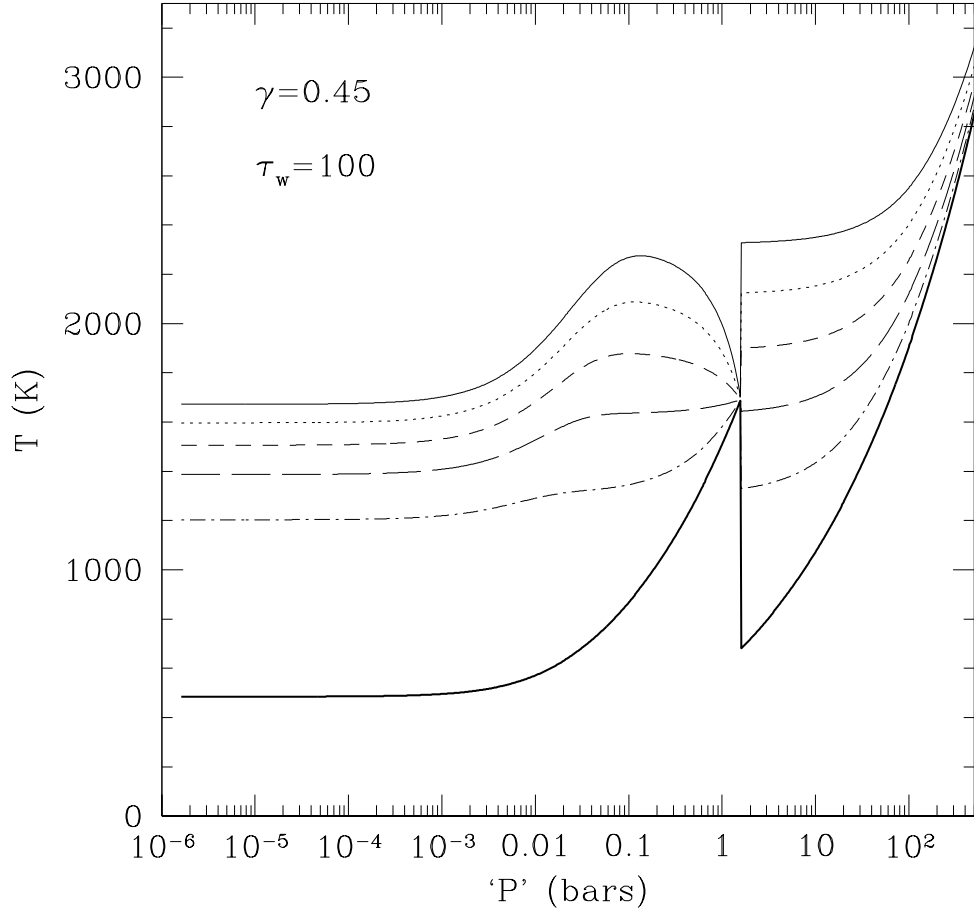


FIG. 22.— The curves show how the temperature profile of the $\gamma = 0.45$ model varies along the equator from center to limb, assuming $\tau_w = 100$. The curves are for values of μ_0 running from 1.0 (top) to 0.0 (bottom), in increments of 0.2. The heavy solid line is the profile at the limb, which also applies on the nonirradiated antistellar side of the planet. We see that the removal of energy by irradiation near the center changes into an injection of energy near the limb and on the antistellar side.

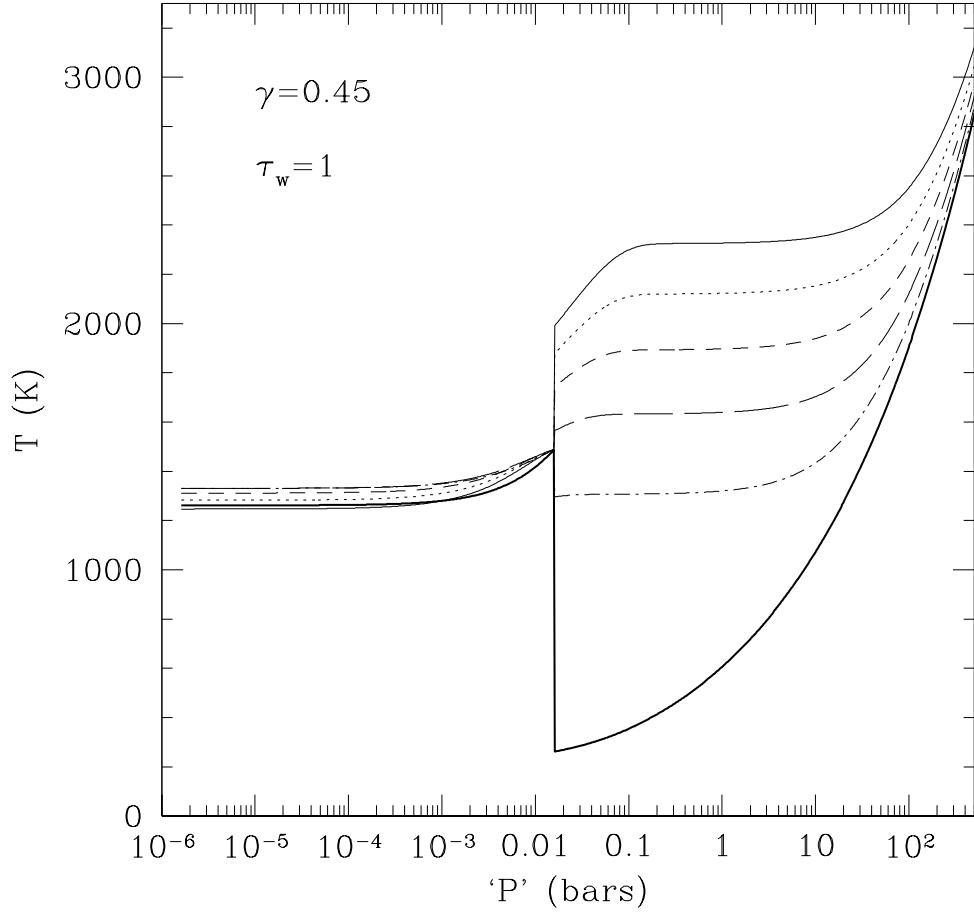


FIG. 23.— The curves show how the temperature profile of the $\gamma = 0.45$ model varies along the equator from center to limb, assuming $\tau_w = 1$. The curves are for values of μ_0 running from 1.0 (top) to 0.0 (bottom), in increments of 0.2. The heavy solid line is the profile at the limb, which also applies on the nonirradiated antistellar side of the planet. We see that the removal of energy by irradiation near the center changes into an injection of energy near the limb and on the antistellar side, with a net result of enforcing a very uniform temperature at lower pressures.

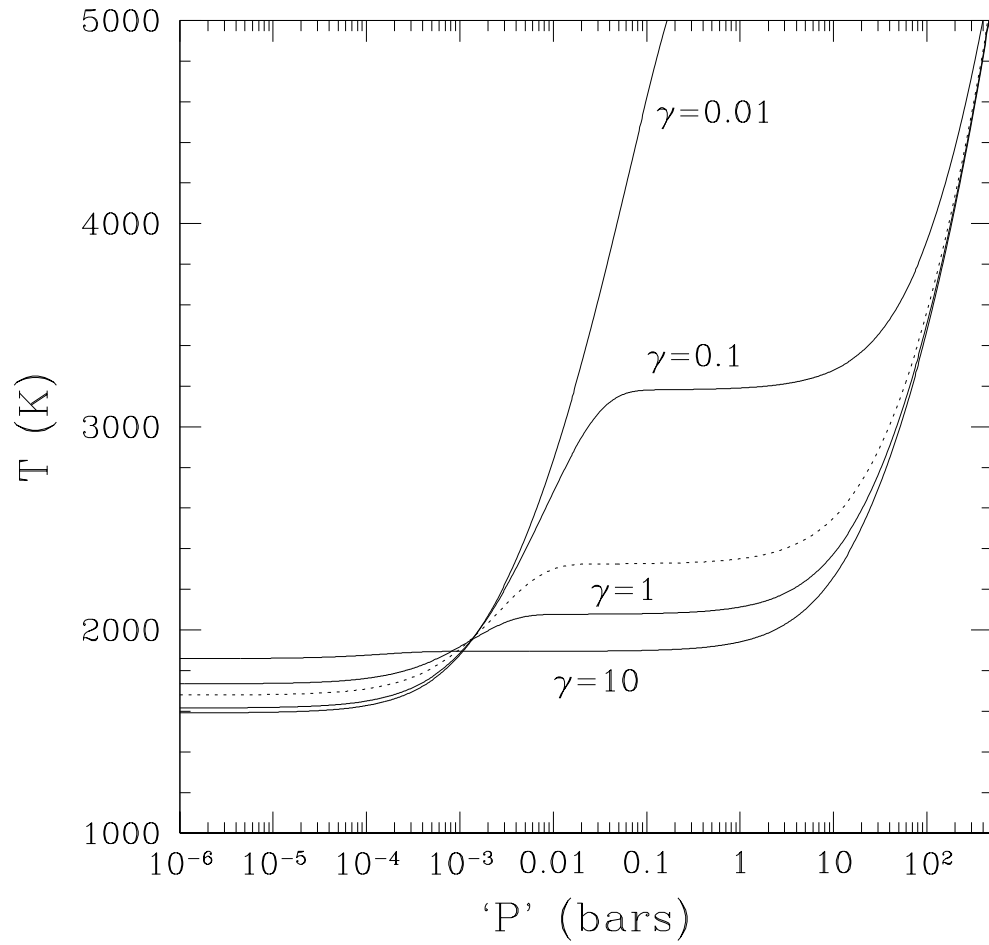


FIG. 24.— The curves show the temperature profiles at the substellar point ($\mu_0 = 1$) as we increase γ from a value of 0.01 to $\gamma = 10$. As γ increases, the incoming energy is absorbed at lower and lower pressures, and the temperature jump decreases, eventually leading to an almost isothermal profile. The dotted line is for the value $\gamma = 0.45$, as calibrated for Figure 20.

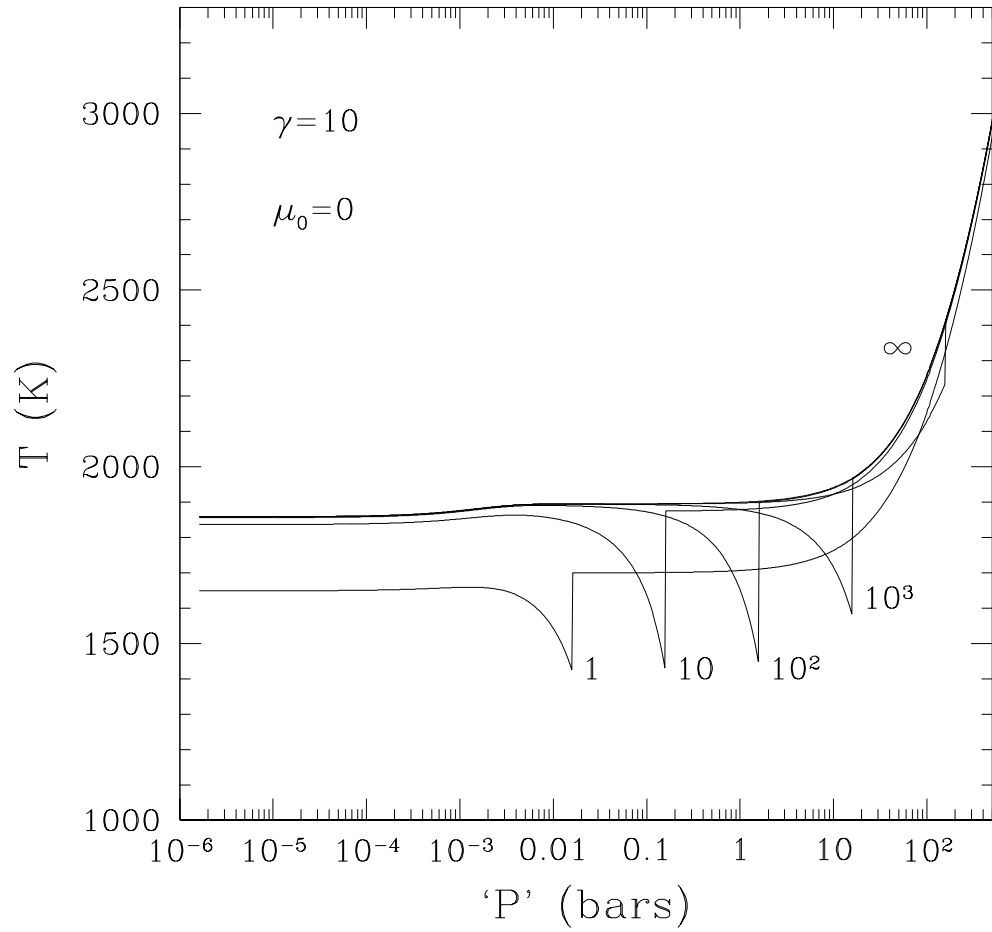


FIG. 25.— Redistribution in the $\gamma = 10$ model is not quite as dramatic, although we still find temperature inversions, which get deeper as τ_w decreases. Recall that $\gamma \sim 10$ and $\tau_w \sim 3$ is a good model for the HD209458b case, suggesting that this atmosphere may have a temperature inversion at the 20 millibar level.